Mechanical shape correlation: a novel integrated digital image correlation approach

Citation for published version (APA):
Kleinendorst, S. M., Hoefnagels, J. P. M., & Geers, M. G. D. (2019). Mechanical shape correlation: a novel integrated digital image correlation approach. *Computer Methods in Applied Mechanics and Engineering*, *345*, 983-1006. https://doi.org/10.1016/j.cma.2018.10.014

Document license:
TAVERNE

DOI:
10.1016/j.cma.2018.10.014

Document status and date:
Published: 01/03/2019

Document Version:
Publisher's PDF, also known as Version of Record (includes final page, issue and volume numbers)

Please check the document version of this publication:

- A submitted manuscript is the version of the article upon submission and before peer-review. There can be important differences between the submitted version and the official published version of record. People interested in the research are advised to contact the author for the final version of the publication, or visit the DOI to the publisher's website.
- The final author version and the galley proof are versions of the publication after peer review.
- The final published version features the final layout of the paper including the volume, issue and page numbers.

Link to publication

General rights
Copyright and moral rights for the publications made accessible in the public portal are retained by the authors and/or other copyright owners and it is a condition of accessing publications that users recognise and abide by the legal requirements associated with these rights.

- Users may download and print one copy of any publication from the public portal for the purpose of private study or research.
- You may not further distribute the material or use it for any profit-making activity or commercial gain
- You may freely distribute the URL identifying the publication in the public portal.

If the publication is distributed under the terms of Article 25fa of the Dutch Copyright Act, indicated by the "Taverne" license above, please follow below link for the End User Agreement:

www.tue.nl/taverne

Take down policy
If you believe that this document breaches copyright please contact us at:

openaccess@tue.nl

providing details and we will investigate your claim.

Download date: 08. Feb. 2024

Available online at www.sciencedirect.com

ScienceDirect

Comput. Methods Appl. Mech. Engrg. 345 (2019) 983–1006

Computer methods in applied mechanics and engineering

www.elsevier.com/locate/cma

Mechanical Shape Correlation: A novel integrated digital image correlation approach

S.M. Kleinendorst, J.P.M. Hoefnagels*, M.G.D. Geers

Eindhoven University of Technology, Department of Mechanical Engineering, The Netherlands

Received 27 February 2018; received in revised form 13 August 2018; accepted 5 October 2018
Available online 26 November 2018

Highlights

- Successful parameter identification from sample contour imaged at arbitrary angle.
- Virtual experiments demonstrate high accuracy in elastoplastic model identification.
- Robust, fast convergence, also for inaccurate viewing angles and binarization.
- Additional inaccuracies in real experiments discussed and partially validated.

Abstract

Mechanical Shape Correlation (MSC) is a novel Integrated Digital Image Correlation (IDIC) based technique used for parameter identification. Digital images taken during an experiment are correlated and coupled to a Finite Element model of the specimen, in order to find the correct parameters in this numerical model. In contrast to regular IDIC techniques, where the images consist of a grayscale speckle pattern applied to the sample, in MSC the images are projections based on the contour lines of the test specimen only. This makes the technique suitable in cases where IDIC cannot be used, e.g., when large deformations and rotations cause parts of the sample to rotate in or out-of-view, or when the speckle pattern degrades due to large or complex deformations, or when application of the pattern is difficult because of small or large specimen dimensions. The method targets problems for which the outline of the specimen is large with respect to the volume of the structure and changes significantly upon deformation. The technique is here applied to virtual experiments with stretchable electronic interconnects, for identification of both elastic and plastic properties. Furthermore, attention is paid to the influence of algorithmic choices and experimental issues. The method reveals good convergence and adequate initial guess robustness. The results are promising and indicate that the method can be used in cases of either large, complex or three-dimensional displacements and rotations on any scale.

Keywords: Mechanical shape correlation; Integrated digital image correlation; Parameter identification; Optimization

---

1. Introduction

Identification and characterization of the mechanical behavior of structures, components and devices is important for design and reliability engineering, e.g., to determine accurate numerical models, to design novel structures or to

---

* Correspondence to: Eindhoven University of Technology, Gemini-Zuid 4.122, 5600MB Eindhoven, The Netherlands.
E-mail address: j.p.m.hoefnagels@tue.nl (J.P.M. Hoefnagels).

https://doi.org/10.1016/j.cma.2018.10.014

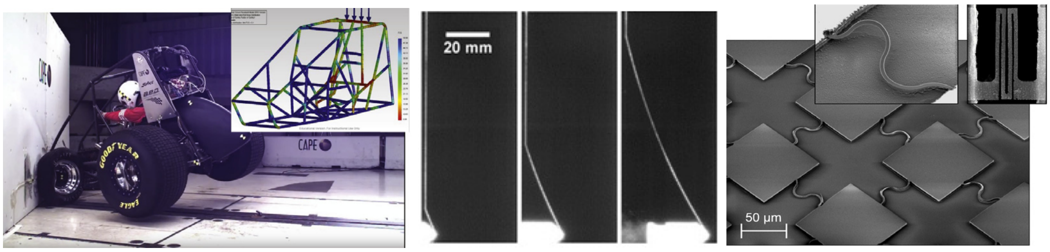

(a) Car safety frame crash test[1] and simulation (Reproduced from [1]).

(b) Projectile wire test (Reprocuced from [2]).

(c) Deforming stretchable electronic interconnects; horseshoe-shaped and rectangular design.

Fig. 1. Examples of deforming structures, ranging from the scale of meters to micrometers, for which it is difficult to apply digital image correlation for mechanical characterization. In Figure (a) an image taken during a crash test with a car frame is depicted. In Figure (b) an image sequence is shown from a ballistic impact test on a single silk fiber. In Figure (c) two examples of stretchable electronic interconnects between rigid (integrated circuit) islands can be seen; a horseshoe-shaped connect from [6] and a rectangular design introduced in [7]. .

monitor structural integrity. A widely used tool for mechanical characterization is digital image correlation (DIC), where deformation of the structure is tracked, usually based on a speckle pattern applied to the object of interest. However, in some cases it is not possible to exploit this technique, for example because pattern application is not feasible. In Fig. 1 several examples are shown for which in situ mechanical characterization is desired, but for which it is difficult to use digital image correlation. All these cases exhibit a distinct contour, which might be used to track the deformations, rather than a speckle pattern applied to the sample. For example, mechanical characterization of the load-bearing structures of cars is important, which can be done with, e.g., crash tests [1], see Fig. 1(a). The material properties depend on the processing history and hence, testing the parts as processed is important to obtain accurate models. Another example, at much smaller scale, is the ballistic impact on a single wire [2–4] or plate [5] in order to detect its high-rate dynamic mechanical properties, see Fig. 1(b). Due to the slender nature of this wire it is difficult to apply a speckle pattern for DIC.

A third example is the stretchable electronic interconnect shown in Fig. 1(c). Stretchable electronics is a topic of increasing interest, with mainly biomedical applications where the flexibility and stretchability provides compatibility between rigid electrical components and soft biological tissue, enabling, e.g., health monitoring [8], flexible devices for cardiac diagnostics [9] and stretchable surgical tools [10]. Recently, a novel design was proposed that consists of freestanding interconnects, which are free to deform three-dimensionally, thus enabling an elastic stretchability beyond 2000% [7]. The stretchable interconnects are integrated in for example miniature sensors used for minimally invasive surgery [11] and hence have microscale dimensions. Because of their small dimensions and complex deformation, DIC based on speckle pattern tracking is difficult to employ. Nonetheless, because of the wire-like form of the stretchable interconnects the outline of the structure is large and changes significantly upon stretching. Therefore, a DIC technique is proposed that is based on the evolving contour of the structure.

DIC approaches can be split in roughly three groups [12]. In local DIC approaches, the image is divided in local subsets, each limited in admissible kinematics (e.g., rigid body motion, shear, uniaxial compression and tension). In the global approach the entire image is correlated at once [13,14]. However, the parametrization of the kinematics should be rich enough to capture the kinematics of the considered experiment, which can be achieved by, e.g., using finite elements (FE) [15] or NURBS shape functions [16,17]. Furthermore, adaptive refinement algorithms were introduced to achieve an optimal set of shape functions for a wide range of problems [18,19].

A third approach is the integrated digital image correlation (IDIC) method, where a mechanical, analytical or finite element model, is used for regularization [12,20,21]. The degrees of freedom are the model parameters. The goal of such an approach is usually to extract material parameters or other model parameters from the experimental images. The method in this paper also follows an integrated approach, where a FE model is coupled to the correlation process.

---

[1] Still from video taken from https://www.capetesting.com/resources/videos/. IMMI and testing division CAPE provided permission to use the image, but where not involved in this research.

The largest difference, however, between IDIC and the proposed Mechanical Shape Correlation (MSC) method is that for MSC contrast in the images is obtained by mapping a signed distance function on the projected contour of the entire specimen, rather than using a grayscale speckle pattern applied to the sample. This projection is based on the outline of the specimen, which changes depending upon the deformation of the sample. This projection can be made for both experimental images and FE simulation results, enabling their correlation. This approach has several advantages. First, the structure is allowed to deform three-dimensionally, since the contour of the sample can still be tracked in projection, while in case of a speckle pattern it is only possible to track in-plane deformation, except when multiple cameras [22,23] or an (optical or atomic force) profilometer [24,25] is used. However, also in these cases the out-of-plane rotation of the sample is still limited, since parts of the structure that rotate out of view (or parts that were not visible in the reference image but rotate into view) cannot be tracked. When correlating images based on the contour of the sample this problem is eliminated. Second, because a speckle pattern is not required, the MSC method can also be applied in cases where pattern application is difficult, such as when the sample dimensions are very small or very large, or when pattern degradation occurs due to large deformations. Therefore, the proposed Mechanical Shape Correlation method provides a solution strategy for integrated DIC problems characterized by large and/or complex, possibly out-of-plane, deformations and cases for which a speckle pattern is not appropriate, as long as the evolving boundary area is significant. The contour is a naturally, always present feature that contains valuable information on the deformations and hence a useful source to base correlation on, especially if other DIC methods or reference point tracking is not easy or possible to employ.

The proposed method shows similarities with Virtual Image Correlation (VIC) [26–28], where also the contour of a specimen is tracked exploiting digital images of the sample. It differs, however, in its goal to identify model parameters versus determining the position of the contour itself, and in the way the real experimental images are compared to virtual ones. In the MSC method, the created signed distance maps for both the experiment and the simulation, enable full-field correlation for which the difference between the images approaches zero, while in VIC the difference is minimized as well, although only in the vicinity of the contour itself, but can never go to zero, since the virtual image is defined in a different manner than the real experimental image.

The paper is organized as follows. In Section 2 the type of images required for MSC is introduced as well as the procedure to obtain them. The images are compared to those used in (Integrated) DIC approaches. In Section 3 the algorithm for solving MSC problems is explained and the differences with a regular IDIC algorithm are highlighted. In Section 4 virtual experiments are performed to demonstrate the Mechanical Shape Correlation method. The stretchable interconnect structure is split to investigate the two main deformation modes separately, both for elastic and elastoplastic material behavior. The influence of some algorithmic choices for MSC is examined. In Section 5 some issues that are to be expected in real experiments are addressed. The paper closes in Section 6 with conclusions.

2. Images

In Digital Image Correlation (DIC), Finite Element Model Updating (FEMU) or Integrated DIC (IDIC), grayscale images (or brightness fields) with a distinct pattern distinguishing individual material points are correlated, see e.g., Fig. 2(a). In contrast, in MSC correlation of the projections of the shape contour of the sample is used instead. This novel technique is based on the assumption that the boundary area is large and the sample shape changes significantly during deformation. In this paper a stretchable electronic interconnect will be investigated, see Fig. 2(b), as a typical example.

The structure of the interconnects consists of several beams connected to each other and hence the boundary length is relatively large. Because of the small dimensions and the proximity of the boundaries, it is difficult to apply a high quality pattern as used in Fig. 2(a). More importantly, because the structures are freestanding and deform out-of-plane upon stretching the patterned area rotates out of view, prohibiting correlation further. In Mechanical Shape Correlation a planar projection of the structure is used as the image. In contrast to regular images, where a region of interest is chosen restricting the correlation to where the pattern is present (red box in Fig. 2(a)), for MSC the region of interest is generally larger than the sample, since the edges are critical for correlation and need to be in view.

The projection can be rendered in different ways. The simplest method is to convert the physical image to a binary image where the background has a different color (e.g., black) than the structure (e.g., white), see Fig. 2(c). However, since large monochromatic areas occur in the binary images, even relatively large deviations from the solution will not result in a high averaged residual and the method will converge before an accurate solution is obtained. Therefore,

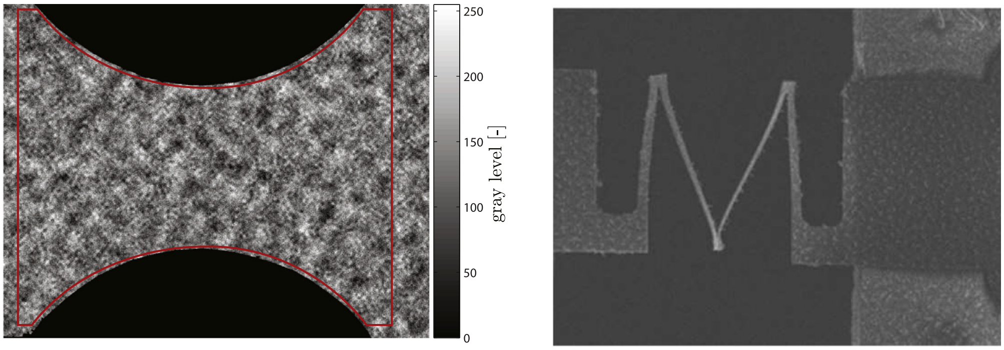

(a) Grayscale pattern

(b) Experimental image of a stretchable electronic interconnect

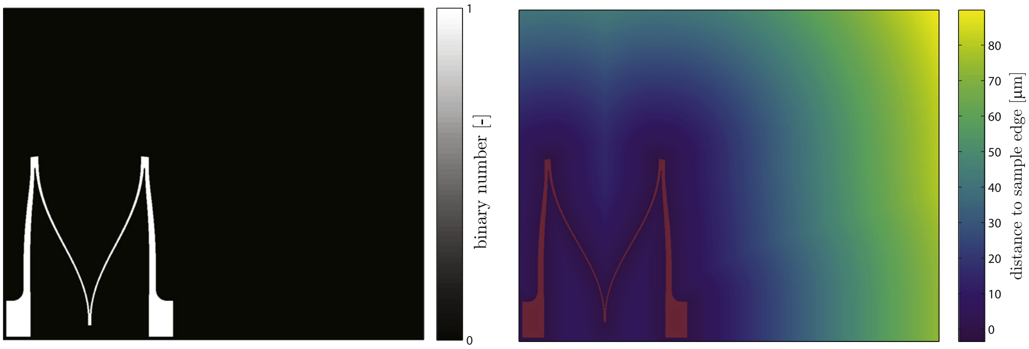

(c) Binary projection

(d) Signed distance map

Fig. 2. Examples of images used for different image correlation techniques. In (a) a dog-bone shaped sample with a grayscale pattern is shown, where the red box indicates the region of interest used for correlation. In Figure (b) a real experimental image of a stretchable electronic interconnect (from [7]) is shown. Figure (c) shows a binary image of the projection of the specimen from (b). In (d) a signed distance map of the same projection is depicted. In orange, the mask used for correlation is shown . (For interpretation of the references to color in this figure legend, the reader is referred to the web version of this article.)

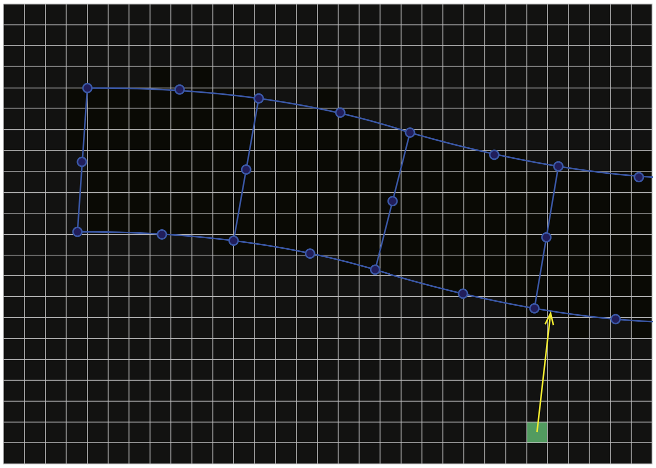

Fig. 3. Extraction of signed distance maps from FE simulation. The element contours and nodal positions are shown in blue and the pixel grid is depicted. For each pixel in the image the shortest distance to this edge is determined and the value is assigned to the pixels, as represented for the one pixel in green . (For interpretation of the references to color in this figure legend, the reader is referred to the web version of this article.)

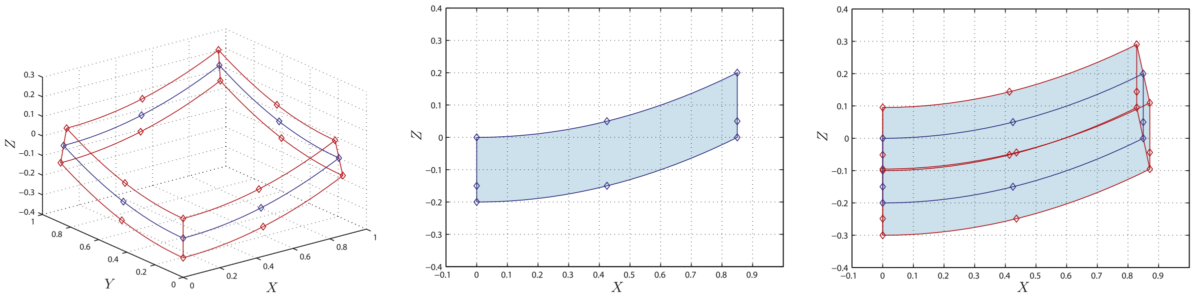

(a) Quadratic shell element

(b) XZ-projection of shell element

(c) XZ-projection corrected for thickness

Fig. 4. An example of a quadratic shell element (with eight nodes) is shown in blue in the left figure. A shell element is infinitely thin and hence the projection (middle figure) will not reveal the thickness of the sample. The thickness is added, see the red element in the left figure, and incorporated in the projection (right figure) . (For interpretation of the references to color in this figure legend, the reader is referred to the web version of this article.)

instead of using binary images, signed distance maps are extracted, see Fig. 2(d). The location of (the projection of) the sample edge is determined and for each pixel the closest distance to this edge is calculated, see Fig. 3. Pixels located inside the structure obtain a negative value, while outside the structure a positive value is assigned. This value is designated to the pixel of the resulting MSC image, further called signed distance map. With this approach a displacement of the sample edge is reflected in a significantly large region in the image.

Likewise, MSC projections need to be made from simulated results using a FE model. Here, care should be taken that the projections created from the FE simulations adequately resemble the reality. For example, when using shell elements in a simulation, the physical thickness of the sample should be properly incorporated. Shell elements are infinitely thin, henceforth, the thickness of the sample is not visible in the FE deformed geometry. The thickness has to be added to the projection, by defining top and bottom surfaces of the element based on the translation and rotation data of the element nodes, as illustrated in Fig. 4.

The images shown in Fig. 2 are all top views from the specimen, i.e., projections on the XY-plane. Evidently, it is possible to make projections from an arbitrary viewpoint, see Fig. 5. If different viewpoints are accessible, one can choose the view that best reflects the deformation of the sample contour, which is beneficial for the correlation. The same viewpoints are to be used in the experiment and simulation. The view direction is represented by the normal vector $\underline{N}$, which is determined by the azimuth and elevation angle. Special cases include the top projection (on the XY-plane) with [azimuth,elevation]= $[0^\circ, 90^\circ]$, the front projection (on the XZ-plane): $[0^\circ, 0^\circ]$, and the side projection (on the YZ-plane): $[90^\circ, 0^\circ]$. The orientation of the resulting image is determined by the vectors $\underline{e}_x$ and $\underline{e}_y$, forming an orthonormal system together with $\underline{N}$. In order to define a unique coordinate system, in this paper we take $\underline{e}_x$ in the XY-plane, and normal to $\underline{N}$. The projection of the three-dimensional structure on the $\underline{e}_x\underline{e}_y$-plane, i.e., the 2D coordinates of all points in the structure along the $\underline{e}_x$ and $\underline{e}_y$ axes, are then determined by taking the inner product of the 3D point coordinates with the vectors $\underline{e}_x$ and $\underline{e}_y$. In DIC literature the image coordinates are usually denoted by $\underline{x}$, or x and y. Note that the image coordinates x and y do not necessarily coincide with the X- and Y-coordinate from the 3D situation in the FE simulation.

Fig. 5 displays simple orthographic projection, where perspective is not taken into account. For most examples in this paper this orthographic projection is used, but it is also possible to substitute projection methods including (weak or full) perspective [29]. In that case additional parameters for the construction of the projected image arise, mainly the 3D position of the camera with respect to the imaged object. The influence of misalignments of the camera angles and position, represented by the distance to the sample along the normal vector $\underline{N}$, is investigated in Section 5.2.

Finally, the structure itself is masked in the signed distance maps, in the sense that the masked pixels are not incorporated in the correlation process, see the orange region in Fig. 2(d). The mask is created by determining which pixels fall inside the closed polygons formed by the projected sample contours. These pixels are designated as the mask. For the experimental images the contour has to be determined using an image segmentation algorithm (see Section 5). Note that when the mask is applied, no negative values exist in the signed distance maps anymore, as only the pixels *inside* the structure, which are now masked, had a negative sign.

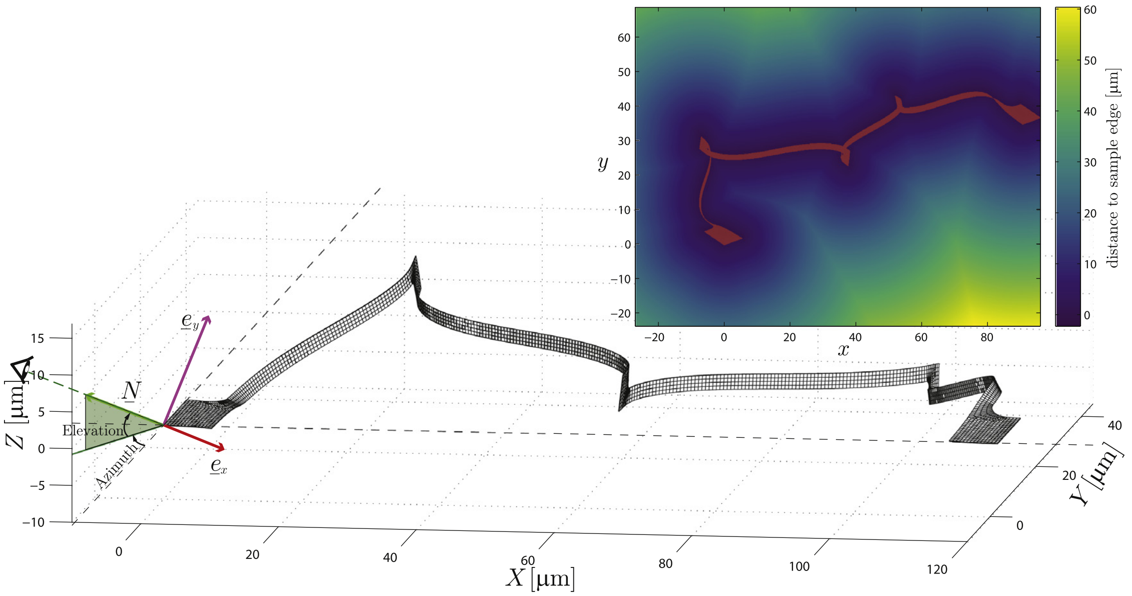

Fig. 5. Projection from an arbitrary viewpoint: The normal vector $\underline{N}$ determining the view is determined by two angles; the azimuth and the elevation. The azimuth is the angle with the negative Y-axis in counterclockwise direction (hence the particular angle shown here is negative) and the elevation is the angle with the XY-plane in positive Z-direction. The projection plane is then determined by vectors $\underline{e}_x$ and $\underline{e}_y$, of which $\underline{e}_x$ is defined such that it lies in the XY-plane. The resulting signed distance map of a stretchable electronic interconnect, including the mask, is shown in the inset for the considered view.

The reason for masking is that it is challenging to determine the closest distance for an inner pixel automatically in a robust manner. The inner pixels are close to multiple segments of the contour (e.g., a side and a top edge) and for slight differences in the FE simulation (due to the iterative process and perturbations on the degrees of freedom, see next section) the closest boundary segment may easily switch, thereby causing jumps in the derivatives of the signed distance maps, which may induce instabilities, affecting correlation. Masking the structure itself is an elegant solution, since correlation is based only on the pixels located outside the structure, for which the closest distance is always to the outer contour of the structure. The effect of masking was investigated in [30],[2] where it was shown that better convergence of the method is achieved when masking the structure.

3. The mechanical shape correlation algorithm

The mechanical shape correlation algorithm is based on integrated digital image correlation (IDIC) [21]. Since a different type of images is used, the algorithm needs adaptation. In this section the algorithm is derived in detail, whereby the differences with the conventional IDIC algorithm are clearly indicated.

Conservation equations

In digital image correlation, multiple images of a sample taken during an experiment are correlated in order to identify displacement fields, strain fields or, in integrated DIC, model parameters. In conventional DIC algorithms, the undeformed image is usually labeled f and a sequence of deformed images defined as g. The algorithm is based on *brightness conservation*, which implies that each material point preserves the same brightness upon deformation, resulting in the same gray value in the image. Mathematically this is denoted

$$f(\underline{x}) - g \circ \underline{\Phi}(\underline{x}, t) = r_{\mathrm{DIC}}(\underline{x}, t) \approx 0, \tag{1}$$

$$\underline{\Phi}(\underline{x}, t) = \underline{x} + \underline{u}(\underline{x}, t), \tag{2}$$

---

[2] Reference [30] is a conference proceeding from the same authors with additional algorithmic details on the masking procedure and its effect on the MSC correlation results.

where $r_{\mathrm{DIC}}(\underline{x}, t)$ are the residual images at each time step t and $u(\underline{x}, t)$ the corresponding displacement field. The notation $g \circ \underline{\Phi}(\underline{x}, t)$ signifies that g applies to the mechanical mapping function $\underline{\Phi}$, which in turn depends on the displacement field $\underline{u}$. This means that the image g is back-transformed to the original coordinates $\underline{x}$ using the function $\underline{\Phi}$, such that the brightness values are in the same position as in image f (if $\underline{u}$ is calculated correctly), making the images comparable.

In mechanical shape correlation, however, this is not possible, since three-dimensional displacements and rotations of a three-dimensional sample are considered. Therefore, in the deformed images, the visible specimen faces may differ from those in view in the reference image. Hence, it is impossible to recreate the reference image from the deformed images by back-deforming them. Therefore, instead of comparing a single undeformed reference image to back-transformed deformed images, images of all increments of the experiment (indicated by g) are correlated to the corresponding images of the FEM simulation (denoted h). The MSC method is schematically shown in Fig. 6. Since the images are created in an equivalent manner from the experimental images and the numerical simulation data, 'brightness', or rather 'distance value' conservation still holds, contrary to Virtual Image Correlation algorithms, where the virtual image is not constructed to exactly match the experimental one [26]. The residual, which thus in theory still approaches zero, can be defined:

$$r(\underline{x}, t) = g(\underline{x}, t) - h(\underline{x}, t) \approx 0, \tag{3}$$

This is now a *forward* transformation, in contrast to the *back*-deformation of images towards the reference situation in DIC. Accordingly, the residual is not defined in the reference configuration, but in the deformed configurations of each increment. Note that both g and h are time (or increment) dependent and not described by brightness values, but by signed distance values to the edge of the sample. Furthermore, note that in regular (I)DIC this forward transformation could also be done. Image h is then described by $h(\underline{x}, t) = f(\underline{x}) \circ \Phi^{-1}(\underline{x}, t)$, where now the inverse mapping function $\underline{\Phi}^{-1}(\underline{x}, t)$ is used, indicating that the images h are created from the reference configuration f using the calculated displacement field $\underline{u}(\underline{x}, t)$ (from the FEM simulation).

Regularization

The DIC problem is intrinsically ill-posed, since the number of unknowns (multidimensional full-field displacements) exceeds the number of equations (equal to the number of pixels in the image). To reduce the number of degrees of freedom (DoFs), the displacement field is regularized. This regularization is usually done by describing the displacement field as a linear combination of shape functions with corresponding coefficients. These shape functions may span local subsets of the total image, as used in local DIC, or the entire region of interest, i.e., global DIC. In integrated DIC, the regularization is achieved by coupling a finite element model of the sample to the correlation, such that the displacement is confined to what is kinematically admissible by the constitutive model. The unknowns are the model parameters that need to be identified. The real mapping function $\underline{\Phi}(\underline{x}, t)$ is approximated by a mapping function that depends on the constitutive parameters $\mathbb{a}$ used in the FE model:

$$\underline{\Phi}(\underline{x}, t) \approx \underline{\phi}(\underline{x}, t, \mathbb{a}). \tag{4}$$

This makes images h also dependent on the model parameters: $h(\underline{x}, t, \mathbb{a})$.

Minimization

In order to find the optimal set of constitutive parameters, similar to other global DIC approaches, the residual is minimized using a least squares approach:

$$\mathbb{a}^{\mathrm{opt}} = \underset{\mathbb{a}}{\mathrm{Argmin}}\, \Psi, \tag{5}$$

with Ψ the objective function, defined as

$$\Psi = \frac{1}{2} \int_{\tau} \int_{\Omega} r^2(\underline{x}, t, \mathbb{a})\, \mathrm{d}\underline{x} \mathrm{d}t = \frac{1}{2} \int_{\tau} \int_{\Omega} \left[g(\underline{x}, t) - h(\underline{x}, t, \mathbb{a}) \right]^2 \mathrm{d}\underline{x} \mathrm{d}t. \tag{6}$$

The solution of (5) implies:

$$\forall j \in [1, m], \quad \Gamma_j(\mathbb{a}^{\mathrm{opt}}) = \frac{\partial \Psi}{\partial a_j}(\mathbb{a}^{\mathrm{opt}}) = 0, \tag{7}$$

with m the number of degrees of freedom

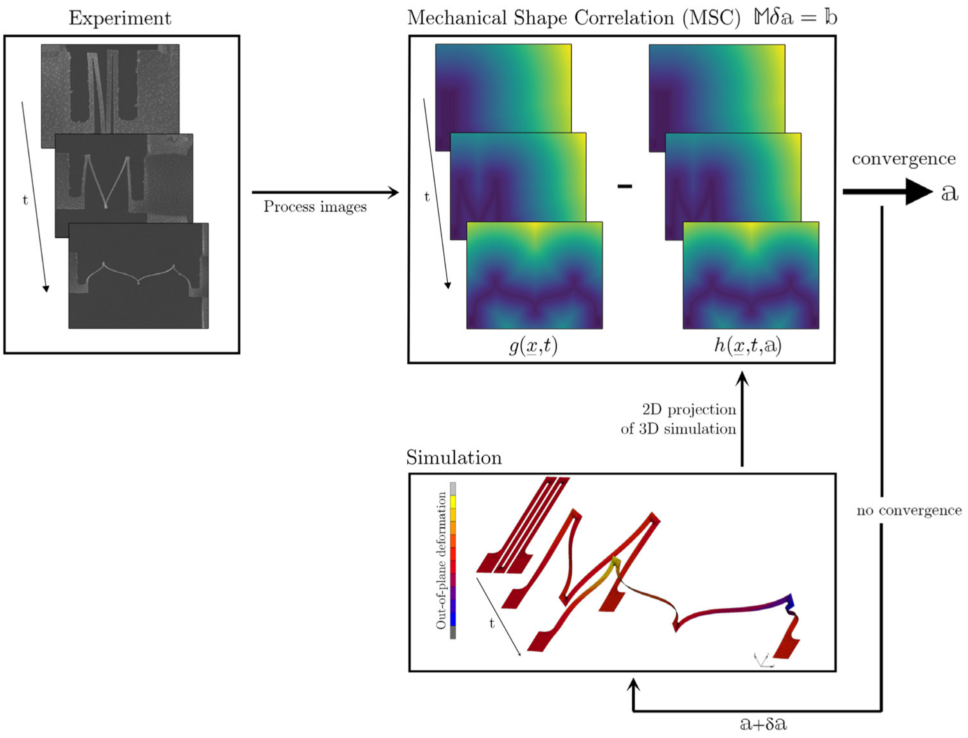

Fig. 6. Schematic representation of the mechanical shape correlation (MSC) method to identify model parameters $\mathbb{a}$ from an experiment. Simulations supply the images h to which the experiment is compared.

Linearization and iterative solving

This problem is non-linear and hence a Gauss–Newton scheme is used to linearize and solve the problem:

$$\Gamma_j^{\text{it}+1} \approx \Gamma_j^{\text{it}} + \sum_{i=1}^{m} \frac{\partial \Gamma_j^{\text{it}}}{\partial a_i} \delta a_i = 0, \tag{8}$$

with $\Gamma_j^{\text{it}} = \Gamma_j(\mathbb{a}^{\text{it}})$. Rewriting this equation gives:

$$\sum_{i=1}^{m} \frac{\partial \Gamma_j^{\text{it}}}{\partial a_i} \delta a_i = -\Gamma_j^{\text{it}} \tag{9}$$

$$\mathbb{M}\delta\mathbb{a} = \mathbb{b}, \tag{10}$$

with $M_{ij} = \frac{\partial \Gamma_j^{\text{it}}}{\partial a_i}$ the components of $\mathbb{M}$.

Right hand side

The right hand side b_j is given by

$$b_j = -\Gamma_j^{\text{it}} = -\frac{\partial \Psi}{\partial a_j}(\mathbb{a}^{\text{it}}). \tag{11}$$

With Ψ given by (6), this becomes

$$b_j = -\frac{1}{2}\frac{\partial}{\partial a_j}\int_\tau \int_\Omega r^2(\underline{x}, t, \mathbb{a}^{\text{it}})\,\mathrm{d}\underline{x}\,\mathrm{d}t = -\int_\tau \int_\Omega r(\underline{x}, t, \mathbb{a}^{\text{it}})\frac{\partial r}{\partial a_j}(\underline{x}, t, \mathbb{a}^{\text{it}})\,\mathrm{d}\underline{x}\,\mathrm{d}t. \tag{12}$$

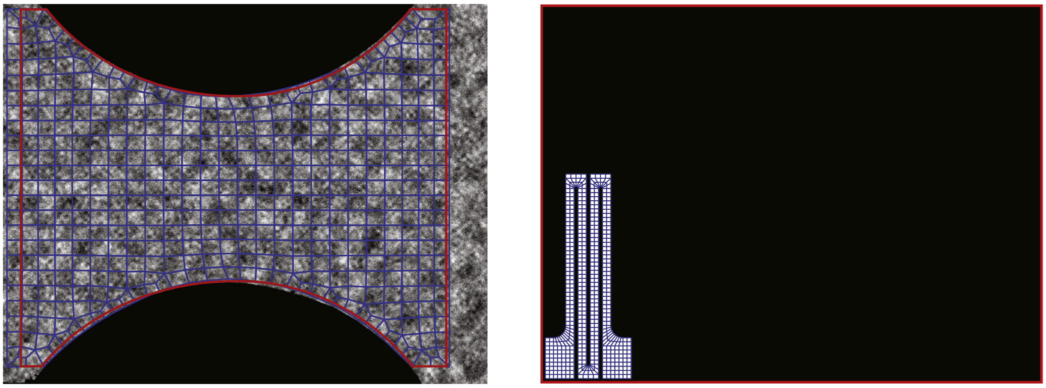

(a) IDIC (b) MSC

Fig. 7. Difference in region where the displacement field is known with respect to the region of interest (ROI) for an IDIC procedure (left) and the MSC method (right). The mesh of the FEM simulation is plotted on top of the image. For IDIC, this is the dogbone sample with a grayscale speckle pattern from Fig. 2(a) and for MSC this is the binary projection of the stretchable interconnect from Fig. 2(c) in the initial configuration. In both images the ROI is displayed by a red outline . (For interpretation of the references to color in this figure legend, the reader is referred to the web version of this article.)

Usually, in IDIC, the derivative of the residual is written as

$$\frac{\partial r_{\mathrm{DIC}}}{\partial a_j}(\underline{x}, t, \mathbb{a}^{\mathrm{it}}) = -\frac{\partial \underline{\phi}}{\partial a_j}(\underline{x}, t, \mathbb{a}^{\mathrm{it}}) \cdot \underline{\mathrm{grad}} g \circ \underline{\phi}(\underline{x}, t, \mathbb{a}^{\mathrm{it}}). \tag{13}$$

The first part, $\frac{\partial \underline{\phi}}{\partial a_j}$, is referred to as *sensitivity maps* $\underline{H}_j(\underline{x}, t, a_j^{\mathrm{it}})$. The second part, $\underline{\mathrm{grad}} g \circ \underline{\phi}(\underline{x}, t, \mathbb{a}^{\mathrm{it}})$, is the *true image gradient* $\underline{G}(\underline{x}, t, \mathbb{a}^{\mathrm{it}})$ [31]. In IDIC, the sensitivity maps are typically calculated using a finite difference scheme:

$$\underline{H}_j(\underline{x}, t, a_j^{\mathrm{it}}) = \frac{\underline{U}^{\mathrm{it}}(\underline{x}, t, a_j^{\mathrm{it}} + \Delta a_j^{\mathrm{it}}) - \underline{U}^{\mathrm{it}}(\underline{x}, t, a_j^{\mathrm{it}})}{\Delta a_j^{\mathrm{it}}}, \tag{14}$$

where $\underline{U}^{\mathrm{it}}$ is the displacement field calculated in the FEM simulation and Δa_j is a perturbation of the jth degree of freedom. The displacements are nodal quantities in FEM calculations and the displacement values need to be interpolated at pixel locations, such that the sensitivity map can be multiplied by the image gradient. For IDIC, the region of interest is smaller than the sample itself (see Fig. 7(a)), i.e., everywhere in the ROI nodes are present for which the displacements calculated in the FEM step are known. Hence, it is possible to interpolate the displacement field at all pixel locations in the ROI. For MSC, however, the region of interest is larger than the sample, see Fig. 7(b), and there is a large area where the displacement field is not calculated. Hence, it is meaningless to extrapolate the displacement field at the pixels outside the sample, whereas the gradient is only known outside the mask, i.e., outside the sample. Therefore, $\frac{\partial r}{\partial a_j}(\underline{x}, t, \mathbb{a}^{\mathrm{it}})$ cannot be calculated by means of the usual splitting into G and H made in IDIC.

Contrary to the displacement field, the residual field $r(\underline{x}, t, \mathbb{a}^{\mathrm{it}})$ is known at all pixel locations naturally, since it is defined as the difference between two images, i.e., the difference between two signed distance maps. Therefore, instead of splitting the residual derivative in the image gradient and the sensitivity map, the derivative of the residual is calculated directly in MSC:

$$\frac{\partial r}{\partial a_j}(\underline{x}, t, \mathbb{a}^{\mathrm{it}}) = \frac{r^{\mathrm{it}}(\underline{x}, t, a_j^{\mathrm{it}} + \Delta a_j^{\mathrm{it}}) - r^{\mathrm{it}}(\underline{x}, t, a_j^{\mathrm{it}})}{\Delta a_j^{\mathrm{it}}}, \tag{15}$$

with

$$r^{\mathrm{it}}(\underline{x}, t, a_j^{\mathrm{it}} + \Delta a_j^{\mathrm{it}}) = g(\underline{x}, t) - h(\underline{x}, t, a_j + \Delta a_j) \tag{16a}$$

$$r^{\mathrm{it}}(\underline{x}, t, a_j^{\mathrm{it}}) = g(\underline{x}, t) - h(\underline{x}, t, a_j). \tag{16b}$$

The step size Δa_j is an important parameter, which could influence the convergence behavior of the method. This perturbation of the degrees of freedom is determined relative to the DoF itself using a perturbation factor P:

$$\Delta a_j^{\mathrm{it}} = P \cdot a_j^{\mathrm{it}}. \tag{17}$$

For the calculation of the derivative of a continuous function using this finite difference scheme, parameter P would ideally be as small as possible, just above numerical accuracy, to ensure an accurate approximation of the derivative. However, in this case the residual is not a continuous function and depends on (non-linear) FE calculations, for which the accuracy is determined by i.a., a set tolerance. If the step size is smaller than appropriate for the given tolerance, the approximated derivative is prone to numerical errors. Therefore, it is important to select a proper value for P, which may be problem specific and it is unfeasible to give a general value for all possible situations. The influence of the step size is investigated in Section 4.

Correlation matrix

The correlation matrix is

$$M_{ij} = \frac{\partial \Gamma_j^{\mathrm{it}}}{\partial a_i} = \frac{\partial}{\partial a_i} \int_\tau \int_\Omega r(\underline{x}, t, \mathbb{a}^{\mathrm{it}}) \frac{\partial r}{\partial a_j}(\mathbb{a}^{\mathrm{it}})\, \mathrm{d}\underline{x}\mathrm{d}t. \tag{18}$$

With the product rule this can be split in two parts: $M_{ij} = M_{ij}^a + M_{ij}^b$, with

$$M_{ij}^a = \int_\tau \int_\Omega \frac{\partial r}{\partial a_i}(\mathbb{a}^{\mathrm{it}}) \frac{\partial r}{\partial a_j}(\mathbb{a}^{\mathrm{it}})\, \mathrm{d}\underline{x}\mathrm{d}t, \tag{19a}$$

$$M_{ij}^b = \int_\tau \int_\Omega r(\underline{x}, t, \mathbb{a}^{\mathrm{it}}) \frac{\partial^2 r}{\partial a_i \partial a_j}(\mathbb{a}^{\mathrm{it}})\, \mathrm{d}\underline{x}\mathrm{d}t. \tag{19b}$$

In the first term, the derivative of the residual appears a second time, which is already determined in (15). In the second term the second derivative of the residual occurs. In literature second order derivatives in the correlation matrix of a DIC algorithm are usually omitted, since it makes correlation highly sensitive to image acquisition noise [31]. Analogously, in this case a high sensitivity to the accuracy of the sample edge detection from the experimental images is expected. Furthermore, the second part contains the residual itself, which, according to [31], is high in the beginning of the correlation and may lead to correlation to a local minimum. Therefore, M_{ij}^b is neglected, effectively using a modified Gauss–Newton scheme as in IDIC. This can be justified, since the residual itself decreases during correlation, and hence, term M_{ij}^b approaches zero upon iteration towards the optimal solution.

Note that the problem is not solved incrementally, but all images (or increments) are lumped into a single minimization process including all data, following [21,32].

Additional residuals

Similar to IDIC, in the MSC framework it is also possible to take into account other experimental data besides the optical part, such as the force history, e.g., [21,33]. This is achieved by defining a second residual, which is the difference between the experimentally measured values and the values resulting from the FEM simulation, which also depend on the degrees of freedom. This residual is independent from the optical residual and hence the total linearized system of equations can be written as a weighted linear combination of the two separate problems. For the examples in this work, however, correlation is based on the optical residual only and no additional data is used.

Boundary conditions in the FE simulation

It is worth noting that it is not straightforward to apply the exact same boundary conditions of the experiment to the FE simulations. It is very important to prescribe the boundary conditions in the FE simulation as accurately as possible, since deviations in them can significantly decrease the accuracy of the correlation. When a part of the sample remains stationary or a known displacement is applied, then these boundary conditions should of course be used for the FE simulation as well. When the boundary conditions are not known for the experiment, it may be possible to implement a

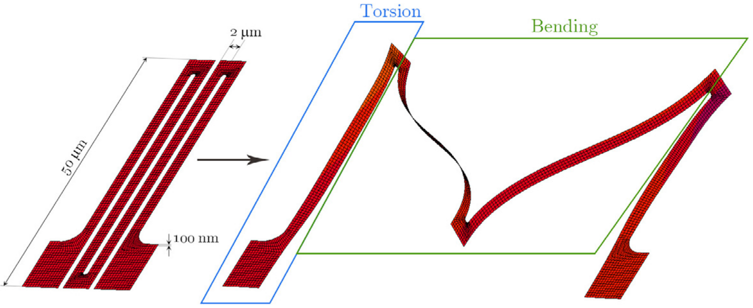

Fig. 8. The deformation of a stretchable electronic interconnect can be split in two main deformation modes: torsion of the outer beams and bending of the middle beams.

pre-step in the correlation algorithm that uses DIC on subregions of the sample relevant for determining the boundary conditions [34,35]. It applies regular DIC (global or local) on these subregions to acquire the displacements, which can be translated to kinematic boundary conditions on nodes in the corresponding subregions in the FE simulation. In case of the stretchable electronics samples considered in this paper, the subregions can be the clamping pads, which do not rotate out of view and are hence suitable for DIC.

4. Virtual experiments

In order to assess the Mechanical Shape Correlation algorithmic performance, several virtual experiments are performed. For the virtual experiments, the experimental images $g(\underline{x}, t)$ do not originate from real experiments, but from a separate finite element (FE) simulation for which the signed distance projections are stored as images g. In this manner, the undesired side effects of a model error or experimental errors (e.g., residual stresses in the sample and image acquisition noise) are eliminated and an exact investigation of the method itself is achieved.

The experiments focus on stretchable electronic interconnects and in particular the structure introduced in [7]. Because of the small dimensions, some mechanical properties are difficult to predict, as they are influenced by size effects. Therefore, it is desired to execute mechanical characterization on the structures as processed. Since these slender wire-like structures exhibit a large evolving boundary area, they form a suitable test case for the MSC method. The deformation of the structures can be described by two main deformation modes: torsion and bending of beams, see Fig. 8. These two deformation modes are investigated separately. The FE simulations for these simplified experiments are less complex and time-consuming than for the full structure and hence more suitable for an analysis of the influence of different parameters in the MSC algorithm, such as the perturbation factor and the initial guess for the unknown model parameters.

First, finite element simulations based on an elastic material model are executed, using quadratic shell elements. The dimensions of the beams are as follows: the length is 50 μm, the width 2 μm and the thickness 100 nm. Later, an elastoplastic material model is used, with two unknown parameters.

4.1. Bending of beams

The deformation of the middle section of the interconnects is characterized by bending of the beams. The virtual experiment is executed by modeling a simplified version of the stretchable interconnects: two connected beams are modeled, of which one is constrained at the end, while the other is lifted by a prescribed load. The deflection of the beams is therefore sensitive to the Young's modulus E.

The objective of this virtual experiment is to recover the correct value for this elastic material parameter E. The Young's modulus that was used in creating all the virtual experiments is 69 GPa (or $6.9 \cdot 10^{-2}$ N/μm^2, since the structure was modeled in microns). The deformation is most pronounced in a side projection of the specimen and hence, YZ-projections are made for the signed distance map images, see Fig. 9. The mechanical shape correlation algorithm is executed for this experiment for different values of the perturbation factor P and different initial guess

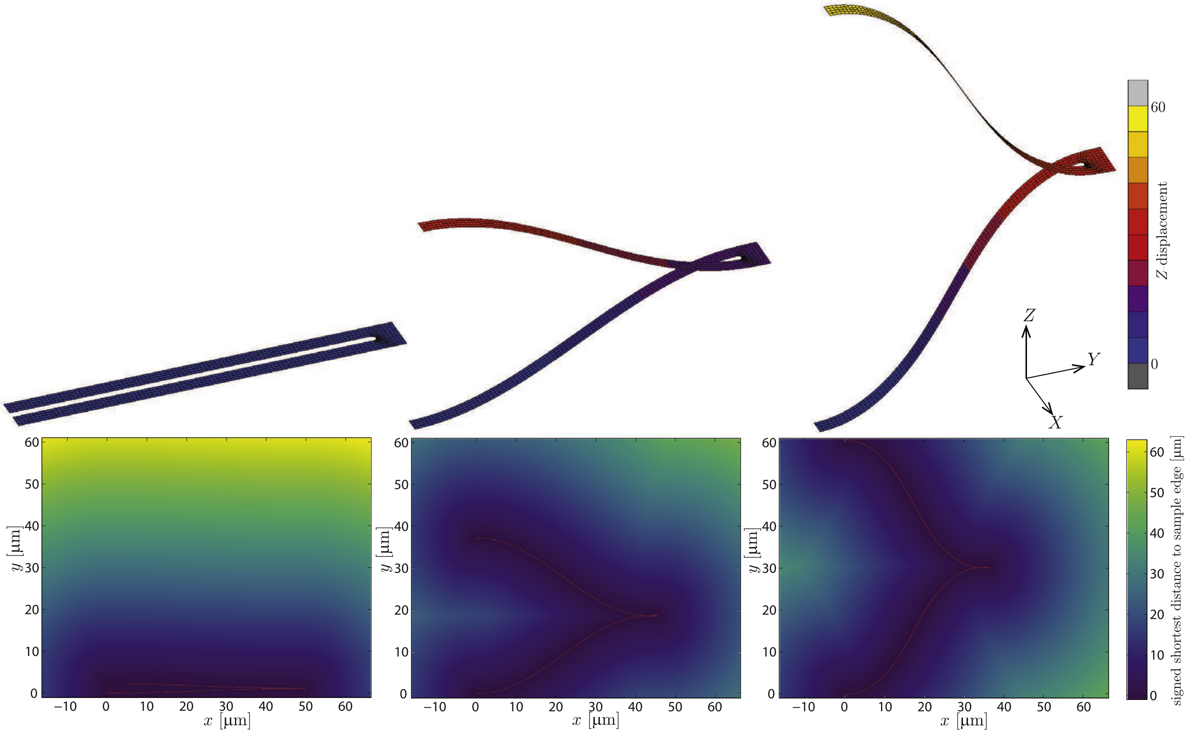

Fig. 9. Signed distance maps for a selection of increments of the virtual experiment for bending of the middle beams. Side projections, on the YZ-plane are made, with projection angles [azimuth,elevation] = [90°, 0°]. Note that the notation for x and y coordinates in the signed distance maps does not correspond to the coordinate system (XYZ) of the FE simulation. In orange the mask used in the correlation is shown on top of the signed distance maps, however, visibility is limited since this is a side projection of the extremely thin beams (100 nm) . (For interpretation of the references to color in this figure legend, the reader is referred to the web version of this article.)

values. For each execution and each iteration the error in the identified Young's modulus is determined:

$$\epsilon_E = \frac{|E - E_p|}{E_p}, \tag{20}$$

with E the value calculated by the algorithm and E_p the solution, i.e., the value used to create the virtual experiment.

The resulting convergence plot is shown in Fig. 10. For a relatively wide range of initial guesses very accurate results are obtained with errors going down to values of 10^{-8}. For even smaller initial guesses, the Young's modulus is so small, that the extreme compliance of the double bending beam structure leads to nonlinear situations that cannot be captured with the considered FE model. Hence, the MSC method cannot be executed, which is indicated by the black circles in Fig. 10(a). For initial guesses above roughly four times the actual value of E the method loses convergence, illustrated by red circles. Note, however, that the MSC algorithm is based on an unbounded Gauss–Newton minimization scheme, which is relatively simple to implement, but might not yield the best results in terms of initial guess robustness. Other minimization approaches, such as Nelder–Mead or modified Gauss–Newton schemes with an update limit and constraints are expected to increase the initial guess robustness even further [36].

The perturbation factor P has a significant effect on the convergence speed, which is most apparent in Fig. 10(b). Too small values ($P = 10^{-7}$) lead to slow convergence. Indeed, the displacement information is only reflected in the location of the sample edge, which is used for creating the images. A very small perturbation induces only a small difference in location of the sample contour and if this difference is smaller than the pixel size it is not manifested in the residual derivative. Consequently, the search direction is not optimal and correlation is slow. Also for a large value of P ($P = 10^{-1}$) correlation is slow, since the derivative of the residual is not calculated accurate enough. For intermediate values of P there is not a large difference in convergence behavior. As mentioned in Section 3, the signed distance maps are smooth and the 'pattern' on the image does not influence the residual and its derivative as much as

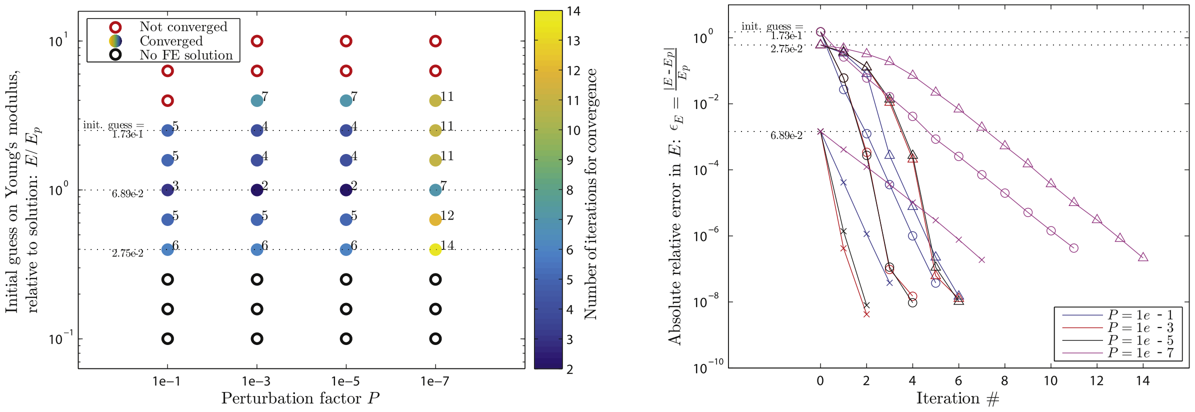

(a) Set of parameters

(b) Convergence plot

Fig. 10. Convergence behavior of the MSC algorithm for the bending beam experiment, for different values of the perturbation factor P and different initial guess values. In figure (a) the initial guess on parameter E (relative to the value used for the virtual experiment E_p) and the perturbation factor P is shown, with for each combination the number of iterations to convergence. For three initial guesses, marked by dotted lines in figure (a), the complete convergence path is shown in figure (b), for all perturbation factors . (For interpretation of the references to color in this figure legend, the reader is referred to the web version of this article.)

the small featured speckle patterns used in IDIC. For this experiment, a proper perturbation factor is in the range of 10^{-5} to 10^{-3}. Note, however, that these values might be problem specific and dependent on the pixel size with respect to the sample dimensions, i.e., the resolution of the images.

4.2. *Torsion of beams*

In the second virtual experiment, torsion of the side beams of the stretchable interconnect is investigated. In Fig. 11 the simulation results are shown. The left side of the beam is clamped and the right side is rotated using a prescribed torque around the X-axis. Therefore, the amount of rotation is dependent on the Young's modulus E. A projection from the side (XZ-projection) is made and the signed distance maps are determined, shown as well in Fig. 11. The FE model used for creating the virtual images is also imported in the MSC procedure, while the Young's modulus E is the unknown parameter.

The convergence plots for the virtual experiments are shown in Fig. 12. The convergence behavior is similar to the first virtual experiment in terms of accuracy and dependence on the perturbation factor. A too small or too large value for P leads to slower, but still adequate, convergence. An intermediate value leads to fast convergence and accurate results. Especially the high accuracy is remarkable, since the difference in specimen contour and hence signed distance maps is small for this experiment, even for large steps in the variable E. Given the definition of the signed distance maps, the information on the edge position is spread through the entire image, which results in a strong sensitivity and hence, a high accuracy.

Again, if the initial guess on the Young's modulus is far too low, stability problems in the FE simulation occur, disabling the MSC algorithm, shown with black circles in Fig. 12(a). The range of initial guesses for which convergence takes place, is smaller to some extent than for the previous experiment. This is due to the smaller differences in sample contour upon changes in E and hence, a lower sensitivity to the material parameter.

4.3. *Elastoplastic bending of beams*

In the previous experiments only one parameter, namely the Young's modulus, was the unknown parameter. To determine this elastic parameter it was necessary to incorporate the load, which was prescribed as a boundary condition in the FE simulation. In a real experiment, measurement of the load may be complex, especially for very large or small structures. For instance, for the small stretchable electronic interconnects, which are designed to be as compliant as possible, it is challenging to measure the force, since it is difficult to design a load cell that is

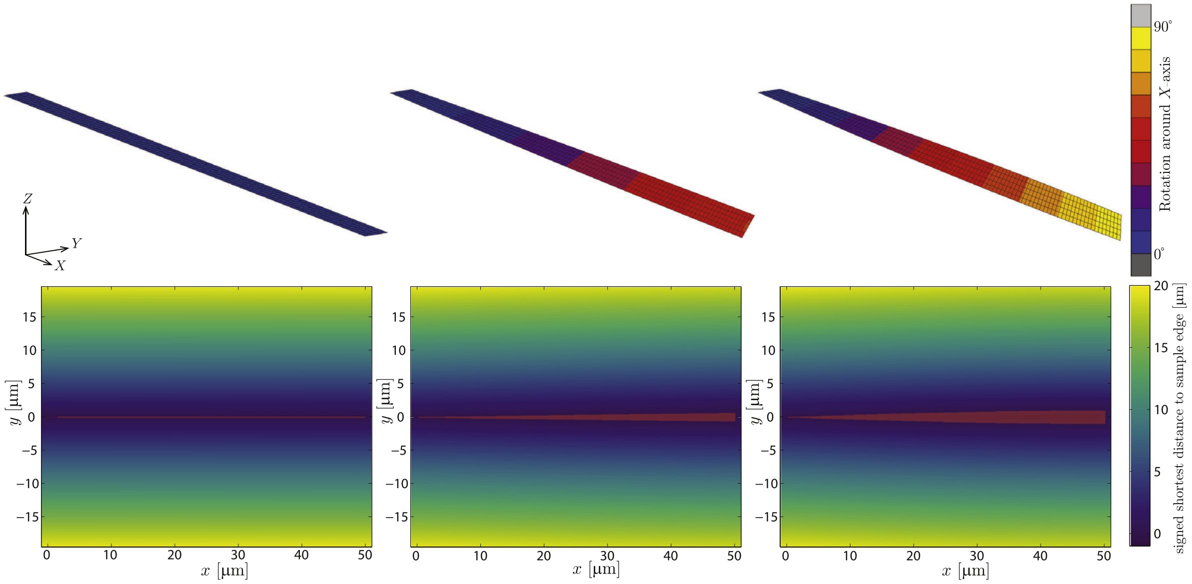

Fig. 11. Signed distance maps for selected increments of the virtual torsion experiment for the side beams. The projection is an XZ-projection, in which the projection angles are [azimuth,elevation] = [0°, 0°]. Note that the notation for x and y coordinates in the signed distance maps does not correspond to the coordinate system (XYZ) of the FE simulation. The mask used in the correlation is shown as well, in orange . (For interpretation of the references to color in this figure legend, the reader is referred to the web version of this article.)

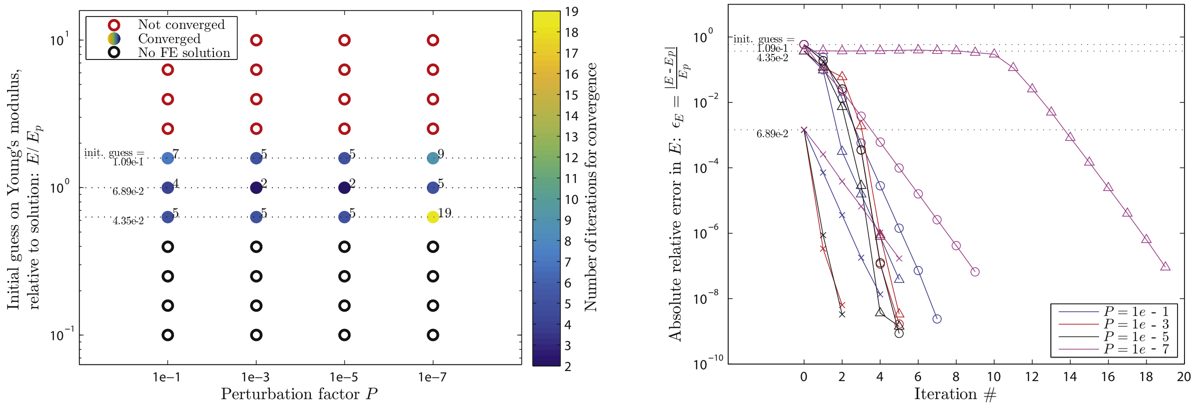

(a) Set of parameters

(b) Convergence plot

Fig. 12. Convergence plot of the MSC algorithm for the torsion beam experiment, for different values of the perturbation factor P and different initial guess values. In figure (a) the set of parameters P and initial guesses on E is shown, with for each combination an indication on the convergence. For three initial guesses the complete convergence path is shown in figure (b), for all perturbations factors.

sensitive enough. Furthermore, the Young's modulus is in general not very sensitive to size effects and therefore in case of these stretchable electronic interconnects not a variable of interest in the Mechanical Shape Correlation procedure. The plastic parameters, such as the yield strength, however, are more important. As was shown in [7], the initial yield strength for these interconnects appears to be much higher in experiments than expected from literature. Hence, the next virtual experiment is focused on identification of plastic parameters. Elastoplastic FEM simulations are performed, where J_2-plasticity is used along with a power law hardening model:

$$\sigma_y = A\left(\varepsilon_0 + \bar{\varepsilon}_p\right)^m, \tag{21}$$

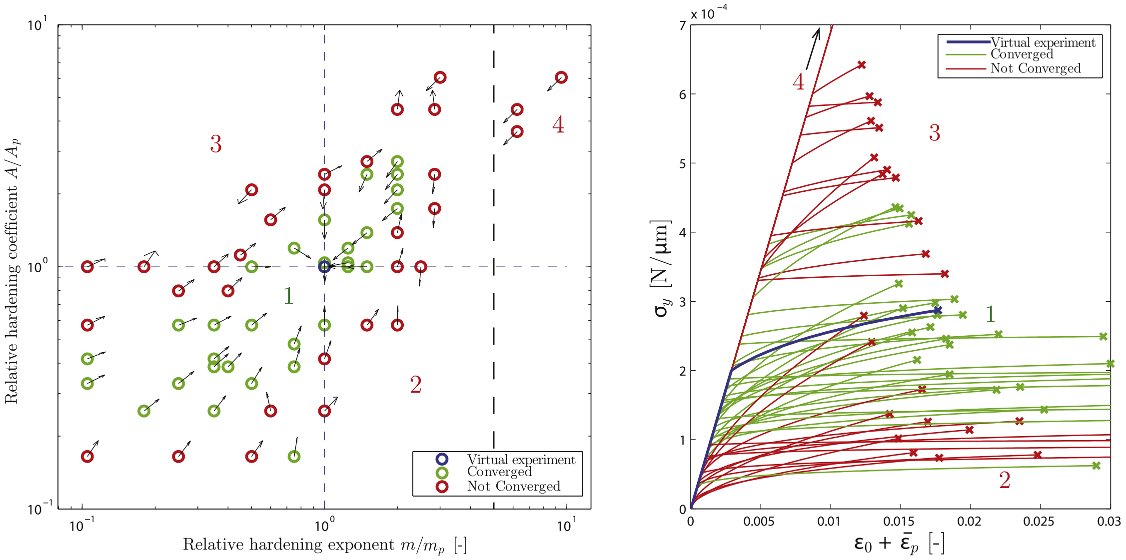

(a) Set of parameters (b) Stress-strain curves

Fig. 13. Plastic parameters, m and A, used as an initial guess for the MSC procedure (left) and corresponding stress–strain curves (right). The parameters are scaled with the values used for the virtual experiment, $m_p = 0.2$ and A_p corresponding to a yield strength of 200 MPa (or $2 \cdot 10^{-4}$N/µm). The blue circle indicates the expected solution. The arrows indicate the direction in which the algorithm is converging or diverging. The stress–strain curves according to Eq. (21) for the parameter combinations are shown on the right. The curves are colored accordingly. The crosses indicate the stress state at the last increment of the FEM simulations. The blue curve corresponds to the virtual experiment with the exact parameter values. Four regimes are indicated by numbers, labeled accordingly in the two figures . (For interpretation of the references to color in this figure legend, the reader is referred to the web version of this article.)

with σ_y the yield stress, ε_0 the strain at initial yield and $\bar{\varepsilon}_p$ the equivalent plastic strain. Parameter A is a coefficient related to the initial yield strength (σ_{y0}) and m is the hardening exponent.

For the virtual experiment an exponential hardening parameter of 0.2 is used and parameter A is chosen such that it corresponds to an initial yield strength of 200 MPa. Coefficient A can be calculated from the initial yield strength using Eq. (21), taking $\bar{\varepsilon}_p = 0$, since there is no plastic strain yet at initial yield, hence: $A = \sigma_{y0}/\varepsilon_0^m$. Furthermore, the strain at initial yield can be described by the end of the elastic region: $\varepsilon_0 = \sigma_{y0}/E$.

Now the displacements of the beam's ends are prescribed, rather than the force. The signed distance maps look similar to those in Fig. 9, although the specimen outline changes slightly when plasticity becomes active, i.e., the beams become slightly more straight and less S-shaped due to the evolving plastic hinge. Based on the previous virtual experiments, a perturbation factor P of $1 \cdot 10^{-3}$ is applied. A range of initial guesses for parameters A and m is used, as shown in Fig. 13(a). In this figure it is also depicted which of the parameter combinations converge to the expected solution and which diverge.

Four regimes emerge in the parameter field (Fig. 13(a)). Regime 1 is located around the diagonal and the algorithm adequately converges for these initial guess values. For these combinations of A and m the initial yield point σ_{y0}, which can be calculated with Eq. (21) for $\bar{\varepsilon}_p = 0$, is typically within a factor of 2 from the initial yield strength of the virtual experiment, see the green curves in Fig. 13(b). Therefore, although parameters A and m differ significantly from the expected values, the initial guess for the yield strength is not very far from the solution and the method converges. For all these converged solutions the error in A and m is reduced to below 10^{-4}.

In the region located underneath the diagonal, i.e., regime 2 in Fig. 13, the initial yield strength is strongly underestimated and hence many of the increments are in the plastic regime, while in the virtual experiment they are in the elastic regime, see the blue curve in Fig. 13(b). Note from the convergence path arrows in Fig. 13(a) that in this regime both A and m increase. Separately this makes sense, since a higher A corresponds to a higher yield strength (for a fixed m) and a higher value for m brings the material behavior in the plastic (hardening) regime closer to the elastic regime. However, since both parameters influence the initial yield strength, σ_{y0} does not change significantly upon increasing both parameters. Because of this dependence both A and m keep increasing and diverge from the solution.

For the parameter combinations above the diagonal the initial yield strength is overestimated, see the red curves of regime 3 in Fig. 13. This implies that a large section of the increments, and hence images, is in the elastic regime, thereby strongly reducing the sensitivity to the plastic parameters. This leads to divergence from the solution.

In the fourth regime the initial guess for m is larger than 1, which is not physical and leads to pure elastic behavior. The same complications as in regime 3 hold and divergence results.

This example illustrates that the problem should be well-defined for the MSC algorithm, which is of course also the case for any IDIC approach. For any method it is difficult to obtain parameters describing the plastic material behavior if there are elastic increments influencing the sensitivity. Therefore, one usually first determines when initial yield occurs and exploits this in the correlation of the material parameters by only using the plastic branch in the correlation. Furthermore, in this case, A and m are interdependent via the initial yield strength σ_{y0}, which can lead to a higher initial guess dependence in the correlation. Also the physical implication of variations in the unknown model parameters should be taken into account. Nevertheless, in a relatively large area in the parameter initial guess field fast convergence towards the correct solution is obtained.

5. Towards real experiments

In this final section the influence of some important aspects that play a role in real experiments is investigated. First, in real experiments the contour of the sample needs to be determined from the images taken during the experiment, while up until now the exact contour was directly extracted from the FE simulation. The method used for extracting the contour from grayscale images may influence the accuracy of the localization of the contour and hence the accuracy of the correlation. Second, in a real experiment it can be difficult to exactly determine the camera viewpoint and a misalignment between the experimental images and the projections from the FE simulations may occur. The influence of this misalignment is investigated.

5.1. *Influence of image segmentation approach*

In this virtual experiment the influence of an important factor affecting real experiments is examined, i.e., the extraction of signed distance maps from pixelized experimental images. This is tested virtually, since in a real experiment the reference solution is unknown and performance assessment is not feasible. Until now the signed distance maps were created directly from the sample contour taken from a finite element simulation. However, in a real experiment grayscale images are taken from the sample, in which the exact edge of the sample is undetermined due to the pixel grid of the image. In other words; a sharp black (for background) and white (for sample) transition is not observed, but around the location of the contour gray pixels occur, since the sample edge crosses these pixels somewhere, see Fig. 14.

To determine the location of the sample edge in a real image, various image segmentation methods with various degree of complexity have been introduced in the literature, e.g. methods based on a level set framework [37,38] or even Virtual Image Correlation algorithms [28]. In contrast, as an ultimate test for the MSC framework, here the most rudimentary method is explored, i.e. imposing a threshold on the gray level to determine which pixel centers belong to the sample and which to the background. This way a binary image is created, from which the now sharp black–white transitions can be used to determine the (approximated) location of the sample edge. The shortest distance to this edge can be calculated for each pixel in the image to create the signed distance map. To mimic this process, in this virtual experiment the signed distance maps are determined as required for an experimental image: create a pixelized binary image first, using the sample contour following from the simulation, and from this image the signed distance map, see Fig. 15. We call this approach the *pixelized* method, whereas for comparison the original method for creating the signed distance maps from the continuous edge (following from the FE simulation in the virtual experiments and from an advanced image segmentation method in real experiments) is named the *continuous* approach. Note that it is not straightforward to choose a proper threshold for real experimental images, especially if illumination (and hence gray level intensity) is not uniform over the image or changes between the images. One should consider if a single threshold value for all images is sufficient, or if a more sophisticated thresholding strategy, e.g., [39], is required. In contrast, creating a binary image from the numerical contour is fairly simple, as it merely includes checking which pixel centers lie inside the contour and which outside, and there is no need to select a proper threshold.

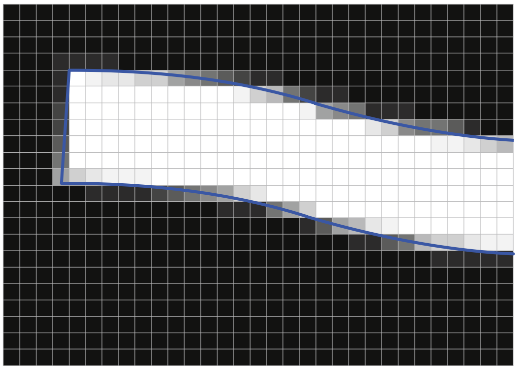

Fig. 14. Impression of an experimental image, where the black–white transition representing the sample edge is smoothed out to gray levels due to the discrete pixel nature of the image. The actual position of the sample edge is represented by the blue line . (For interpretation of the references to color in this figure legend, the reader is referred to the web version of this article.)

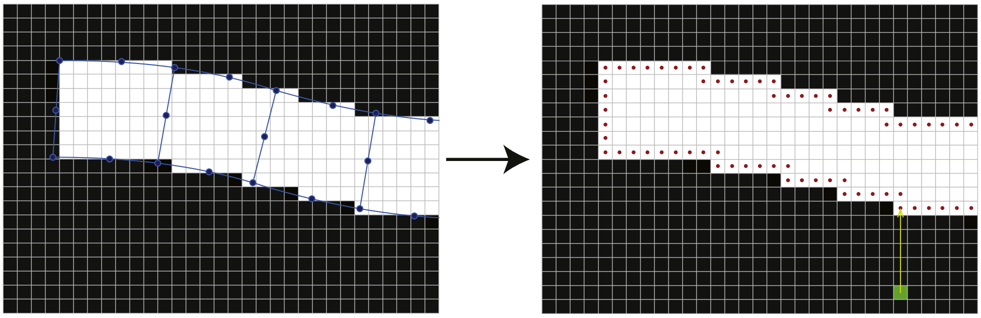

Fig. 15. Creating signed distance maps via the two stage pixelized approach. The pixel grid of the image is shown and the blue lines represent the element contour as obtained from the simulation. A pixelized binary image is created by determining which pixels are located within this contour, to mimic the effect of the most rudimentary image segmentation method, i.e. imposing a gray level threshold, on a real experimental image; the resulting edge is indicated with red dots. In a second step that is specific for the MSC method, the signed distance map is created based on the pre-allocated edge, as is shown for one pixel . (For interpretation of the references to color in this figure legend, the reader is referred to the web version of this article.)

The influence of using the pixelized method, is investigated here, on the virtual experiment from Fig. 9, with an elastic material model with the Young's modulus E as material parameter, as in Section 4.1. In Fig. 16(a) the residual field is shown for one of the increments of the double bending beam experiment, where images g and h are calculated with the pixelized approach. In this residual field lines perpendicular to the structure are observed. Fig. 17(a) reveals the origin of these lines. Creating the binary image first induces a shift of the edge in the order of a couple of pixels. Therefore, the difference in signed distance value for pixels positioned in a line perpendicular to the edge around the location of this shift, for a small dislocation of the element contour, is relatively high for the pixelized approach compared to the continuous method (Fig. 17(b)). This difference becomes visible when the images are subtracted, i.e., the residual is calculated.

In the derivative of the residual these lines become even more apparent, see Figs. 16(b) and 16(c). Especially for a small perturbation factor the lines dominate the derivative field, which may lead to poor or slow convergence. This is indeed observed in the convergence plots in Fig. 18, where the MSC algorithm is executed for initial guesses within the converging domain of Section 4.1 and the three best perturbation factors. The decrease in convergence performance is larger if the perturbation factor is smaller. The initial guess is not as important. The pixelized approach also impairs the final accuracy of the method, i.e., the error after the final iteration is larger. It is important to note, however, that even when using the most rudimentary image segmentation method, the MSC method still converges within a reasonable amount of iterations (for acceptable values of the perturbation factor) with an accuracy of 10^{-4}, which is a promising result for correlations incorporating this experimental issue. In real experiments, however, other

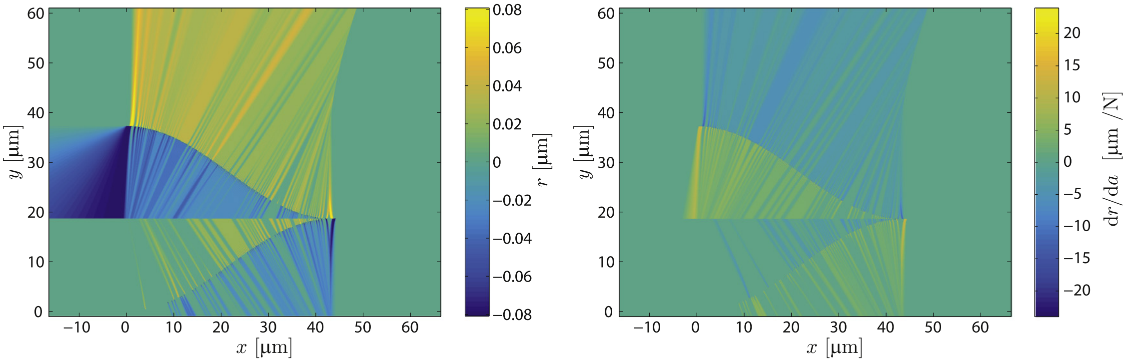

(a) Residual field

(b) Residual derivative, $P = 1e - 3$, pixelized

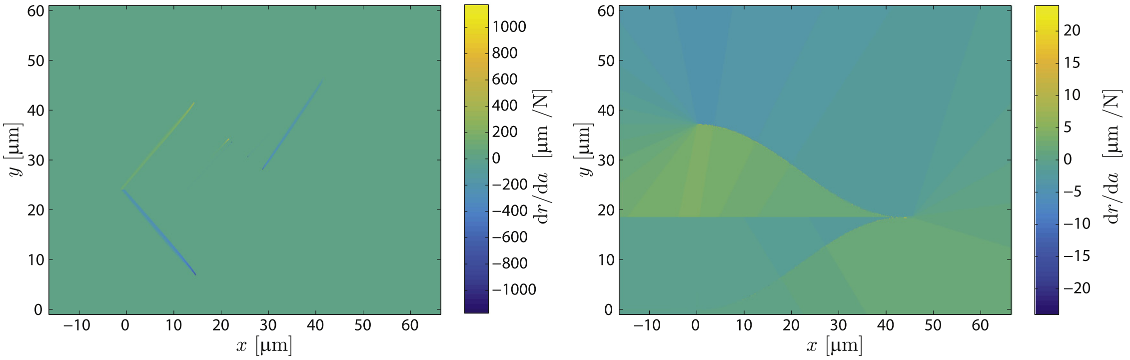

(c) Residual derivative, $P = 1e - 5$, pixelized

(d) Residual derivative, $P = 1e - 3$, continuous

Fig. 16. Residual field and derivative of the residual, as calculated with Eq. (15), for one of the increments of the virtual bending beams experiment. The images are created using the pixelized approach for the signed distance maps for Figures (a)–(c). The derivative is calculated for Δa_i with a perturbation factor of $1e - 3$ and $1e - 5$. The large difference in scale for Figures (b) and (c) occurs due to the difference in order of magnitude in Δa_i, while the derivative is calculated by dividing by this number. In Figure (d) the residual derivative is shown for which the images are created with the continuous approach.

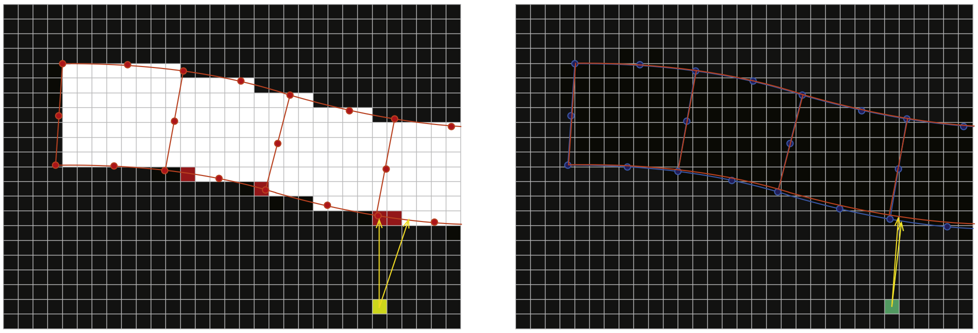

(a) Pixelized approach

(b) Continuous approach

Fig. 17. Construction of signed distance map for a slightly displaced, due to the update and perturbation of the DoFs, element contour. For the pixelized method (left) the pixels that were located within the edge in the original configuration of Fig. 3, but not inside the displaced edge are marked red. For comparison, for continuous approach (right) the original element contour (blue) and the displaced edge (orange) are also depicted. In both figures the arrows indicate the closest distance to the binary edge in the original situation and the displaced configuration . (For interpretation of the references to color in this figure legend, the reader is referred to the web version of this article.)

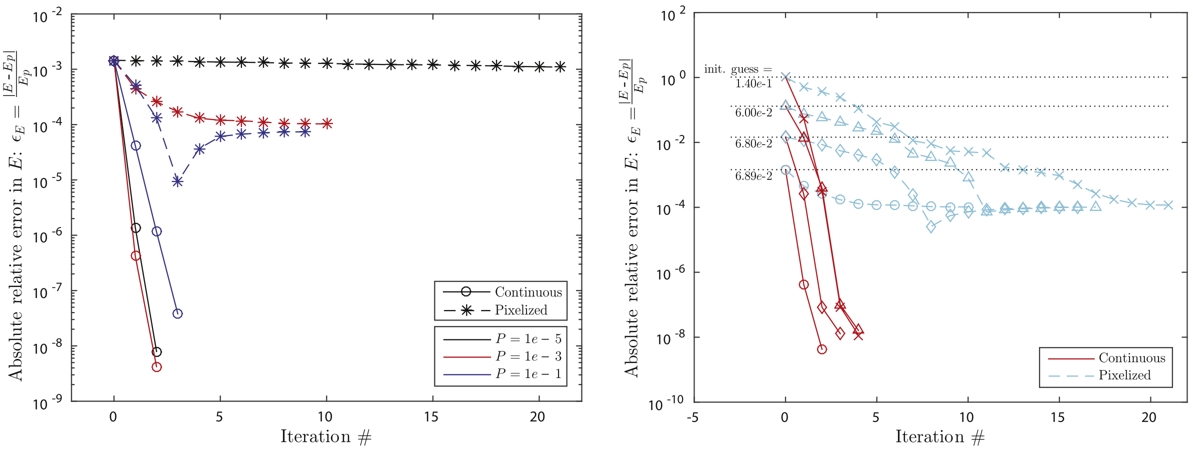

(a) Variation of P (b) Variation of initial guess, $P = 1e-3$

Fig. 18. Convergence plots of the MSC algorithm for the bending beam experiment. A comparison is made between the continuous approach and the pixelized method for creating signed distance maps. The perturbation factor P is varied, as well as the initial guess.

experimental issues play a role as well and a basic image segmentation method such as binarization may not be adequate to obtain (accurate) correlation and another, more advanced, algorithm might be necessary.

As mentioned before, a possibility for segmenting the image, i.e., differentiating the sample from the background, is a Chan–Vese algorithm [37,38]. The contour and signed distance map (level sets) following from this algorithm are shown on the left side of Fig. 19 for a SEM image of a real experiment with the stretchable electronic interconnects from [7]. The Chan–Vese algorithm has two penalty parameters, μ and ν to penalize the length of the curve and the area inside the curve respectively. They can be fine-tuned to make the curve smoother. In Fig. 19(a) and (b) the obtained curve and signed distance map with ($\mu = 0.05$, $\nu = 0.1$) and without ($\mu = \nu = 0$) penalties on the curve length and area are shown. Indeed, the curve where the penalty factors are non-zero is smoother, while the other curve appears wavering because it follows the small "fur-like" features on the surface of the interconnect [40] that are located at the edges. In fact, while these "fur-like" features do not affect the interconnect mechanics, they do significantly alter the signed distance map. Therefore, the micro-fabrication processing should be improved first before a MSC parameter identification on these interconnects can be performed. Nevertheless, a comparison is made with the signed distance maps obtained from numerical simulations. To this end, on the right side of Fig. 19 the contours and signed distance maps from simulation results are shown. In Fig. 19(c) the signed distance map is directly made from the top, bottom and side contours following the FE simulation, consistent with the continuous approach of Fig. 3 (the binary image behind the contour of Figure (c) is only shown for visualization purpose, but not used to construct the signed distance map). Note that the resulting signed distance map looks non-smooth at the edges, which is a result of the construction of the signed distance map with a double (top and bottom) contour and a reason to mask out these pixels in the correlation process, as discussed in Section 2. The contour (and hence signed distance map) looks significantly different from the ones in Fig. 19(a) and (b). Besides the simplistic pixelized approach introduced above, another, better, method to make the numerical image correspond to the real one better is to first create a high resolution binary image (e.g., a ten times higher resolution than the experimental image) and then decrease the resolution to the level of the experimental image, whereby the sharp black–white transition is smoothed, thereby mimicking the image capture process of a CCD camera. Then the same Chan–Vese algorithm can be applied to this gray-level image to obtain a similar contour and signed distance map as from the real experimental image. The result of this is shown in Fig. 19(d). As the correct plasticity parameters are unknown, the overall shape of the interconnect is different between experiment and simulation, which makes a quantitative comparison impossible. Moreover, the signed distance maps of Fig. 19(b) and (d) are clearly different at the locations of the "fur-like" features. However, from qualitative analysis of a region of a clean edge without these features it is concluded that, for the same Chan–Vese settings, a good resemblance is obtained for the detected edge, in terms of a similar slightly wavy edge and a similar slight short-cut of the edge in the inner corner. Therefore, it is believed that, in absence of "fur-like" features and with further research to select the optimal values of the Chan–Vese penalty parameters, it should be possible to obtain highly similar signed distance maps that are suitable for correlation.

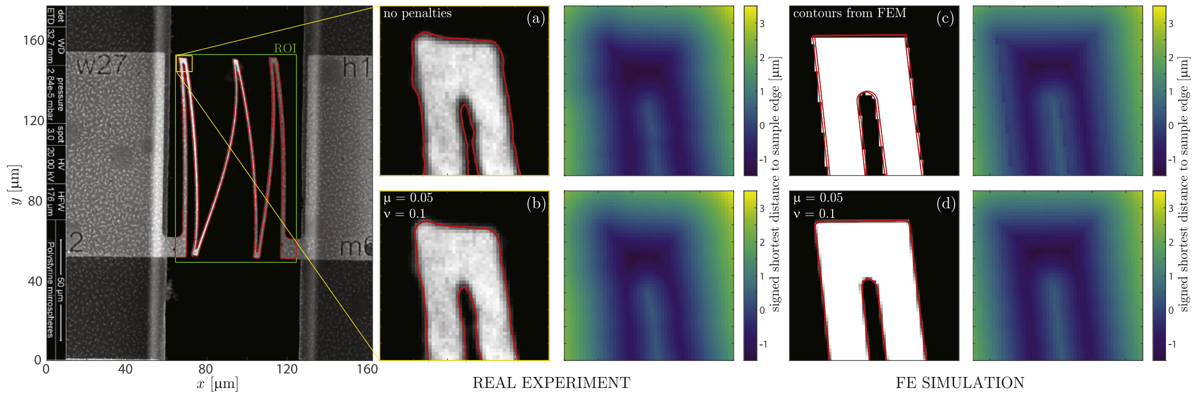

Fig. 19. Comparison of contours and corresponding signed distance maps obtained from a real experimental (SEM) image and from an FE simulation. For the real experimental image a Chan–Vese algorithm is used to segment the image (figures (a) and (b)), where μ and ν are penalty parameters on the curve length and the area inside the curve respectively, which can be adjusted to obtain a smoother curve. For the numerical images a signed distance map is made directly from the (top and bottom) contours following the simulation (figure (c)) and with the same Chan–Vese algorithm, after mimicking a real experimental image from the simulated contours (figure (d)).

Table 1

Error in parameter E (according to Eq. (20)) after correlation with misaligned projection angles. The true angles, [azimuth,elevation]= [−81.2°, 40.2°], are highlighted in the table. Note that the middle dark blue highlighted value is the error without misalignment.

azimuth \elevation	36.2°	39.2°	40.2°	41.2°	44.2°
−85.2°	$1.1 \cdot 10^{-4}$	$4.7 \cdot 10^{-2}$	$6.2 \cdot 10^{-2}$	$8.0 \cdot 10^{-2}$	$1.3 \cdot 10^{-1}$
−82.2°	$4.5 \cdot 10^{-2}$	$4.4 \cdot 10^{-5}$	$1.6 \cdot 10^{-2}$	$3.3 \cdot 10^{-2}$	$8.5 \cdot 10^{-2}$
−81.2°	$5.8 \cdot 10^{-2}$	$1.6 \cdot 10^{-2}$	$3.8 \cdot 10^{-6}$	$1.7 \cdot 10^{-2}$	$6.9 \cdot 10^{-2}$
−80.2°	$7.7 \cdot 10^{-2}$	$3.2 \cdot 10^{-2}$	$1.8 \cdot 10^{-2}$	$3.8 \cdot 10^{-5}$	$5.2 \cdot 10^{-2}$
−77.2°	$1.3 \cdot 10^{-1}$	$8.3 \cdot 10^{-2}$	$6.8 \cdot 10^{-2}$	$5.1 \cdot 10^{-2}$	$6.1 \cdot 10^{-4}$

5.2. *Influence of camera misalignment*

Another problem that might arise during real experiments includes inexact agreement between the view of the camera in the experimental setup and the projection angle for the FE simulation. Here the influence of an error in the projection angles and camera position is investigated and a solution is posed. Also, the role of perspective is addressed.

Again, the virtual experiment with the double bending beams with one elastic unknown parameter from Section 4.1 is repeated, but now the images are made under an angle instead of the exact YZ-projection. The correlation is performed with an initial guess within the converging regime (Fig. 10): $E = 10^{-0.2} \cdot E_p$, where E_p is the solution, and a perturbation factor of $P = 1e-3$. In the virtual experiment the azimuth and elevation angles are chosen −81.2° and 40.2° respectively. The correlation is performed for a misalignment in these angles up to 4°, which is a generous upper bound of the inaccuracy with which the viewing angle in a real experiment can be determined. The resulting errors in the objective parameter E are listed in Table 1. It can be seen that even for large misalignment the algorithm still converges towards the solution. The error in the Young's modulus is naturally not as small as with a perfectly aligned system, however, it is still reasonable.

Besides accepting the error occurring due to misalignment, it is also possible to incorporate the projection angles as additional unknown parameters in the correlation procedure. To test this, the same virtual experiment is executed, and moreover, perspective is included in the projection as well. The difference between the before used orthographic projection and a projection where perspective is used is shown in Fig. 20(a). This introduces another degree of freedom, namely the position of the camera, which is here defined as the distance of the camera to the object along the normal to the projection plane (which is specified by the projection angles). Hence, this virtual experiment has four unknown parameters, i.e., Young's modulus E, azimuth angle θ_{az}, elevation angle θ_{el} and camera distance d_c. In

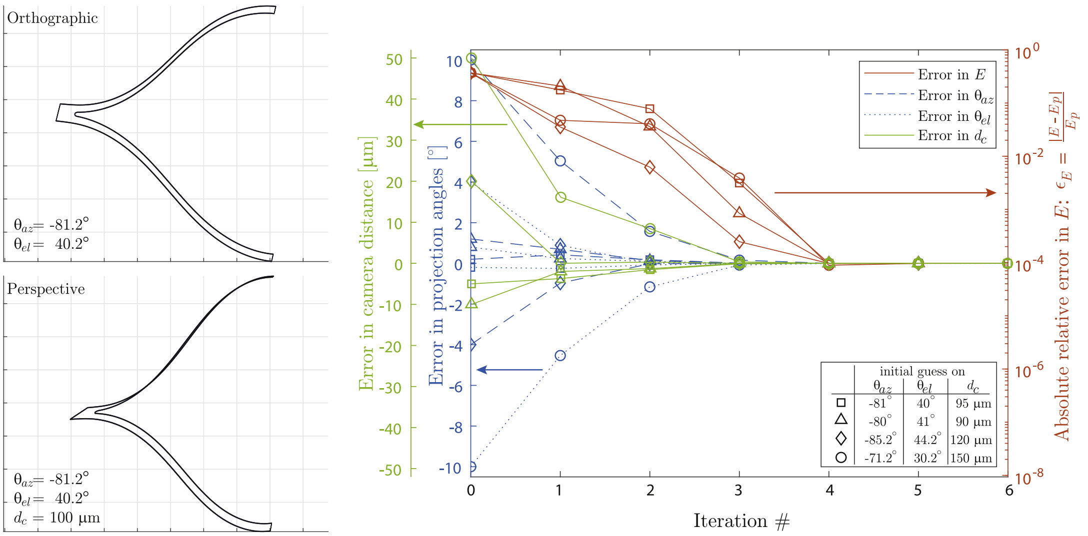

(a) Projections of double bending beam (b) Convergence plot

Fig. 20. Difference between an orthogonal and perspective projection and convergence plot for the virtual experiment with projection angles as additional unknown parameters. The virtual experiment is repeated for four different initial guesses on the projection angles and camera distance, as listed in the inset table in the right figure. The decrease in error is plotted for all four parameters in the correlation process, i.e., E, θ_{az}, θ_{el} and d_c. For E the error is calculated by Eq. (20). For the projection angles and camera distance the error is given as the difference in degrees and micrometer respectively between the calculated values and the actual values ($\theta_{az} = -81.2°$, $\theta_{el} = 40.2°$, $d_c = 100$μm).

the case of the viewpoint parameters the sensitivity maps, i.e., residual derivatives, are not determined by performing an extra FE simulation with perturbed parameters, but by directly creating new signed distance maps (and from these the residuals and their derivatives) with perturbed projection angles and camera distance. In the virtual experiment four different initial guesses on the azimuth and elevation angles, ranging from a misalignment of 0.2° up to 10° and on the camera distance, ranging from 5 μm to 50 μm (in comparison, the sample itself is 50 μm in length) are assessed. The initial guess on the Young's modulus is the same for each experiment ($10^{-0.2}$ times solution E_p) and the perturbation factor is again $1e - 3$. The resulting convergence behavior is presented in Fig. 20(b). It can be seen that even for a large initial misalignment, i.e., 10° error in the projection angles and 50 μm error in the camera position, the correct solution is found within a small amount of iterations and with high accuracy (order 10^{-4}). This leads to the expectation that in application to real experiments, where the camera view can in general be estimated within $\sim 1°$, the material parameters can still be determined accurately, especially if the camera viewpoint specification is included as additional unknowns in the correlation procedure.

5.3. *Other experimental imaging issues*

Imaging can induce many other error sources for image correlation algorithms, for instance changes in illumination, lens aberrations and scanning artifacts (when using a scanning electron microscope). Their influence may be smaller or larger, depending on the problem and the specific experimental conditions, and is worth investigating case-specifically. Some issues can be assessed beforehand and corrected for manually. Others can be addressed by adding representative parameters as degrees of freedom in the correlation, similar to the projection angles above, or the digital image correlation framework could be extended with model functions for the distortions to correct for them, such as has been done for electron microscopy artifacts like spatial distortion, drift distortion and scan line shifts [41,42].

6. Conclusions

A novel mechanical identification method, Mechanical Shape Correlation (MSC), has been proposed in this paper. The algorithm is based on Integrated Digital Image Correlation methods, where images taken during an experiment are coupled to a Finite Element model in order to determine correct model parameters. In regular (I)DIC methods a speckle pattern is applied to the sample and correlation of the images is based on the brightness conservation of the pattern. Accordingly, correlation is only possible if the patterned area remains in view and hence large rotations are not permitted. Also, complex and large deformations may lead to severe degradation of the speckle pattern, which inhibits correlation. Furthermore, speckle pattern application can be challenging when dealing with, for instance, specimens of very small or large dimensions. In the MSC method, the images do not consist of a grayscale speckle pattern, but they are projections of the sample, based only on the contour of the structure. The advantage is that complex, three-dimensional deformations form no obstacle for correlation, since the outline of the specimen can be tracked nonetheless. This is beneficial in cases where such complicated displacement fields occur, but also in cases when it is not possible to apply a speckle pattern. Condition is, however, that the specimen of structure outline changes sufficiently during deformation of the sample.

In this work, the method is applied to virtual experiments on stretchable electronic interconnects, consisting of multiple beams connected to each other. The deformation of the stretchable interconnects is described by two main modes: double bending of the middle beams and torsion of the outer beams. These two deformation modes were analyzed separately and the effect of several algorithmic variables, such as the perturbation factor and the initial guess, was investigated. This was done for an elastic material model with a single unknown parameter, as well as for an elastoplastic power law hardening model with two unknown model parameters, the hardening coefficient A and the hardening exponent m.

In all virtual experiments fast and accurate convergence was obtained within a certain range of initial guesses, which is due to the nature of the signed distance maps, which span the entire image, despite that in the projections the deformations are only reflected in the sample contour instead of the entire sample surface. The perturbation factor, which influences the update in the finite difference approach for calculating the sensitivity of the residual towards the degree(s) of freedom, i.e., the unknown model parameter(s), affects the convergence behavior. A proper perturbation factor for the considered experiments was found to be in the order of 10^{-5} to 10^{-3}. The initial guess regime for which the method converged ranged from two to three times smaller values than the expected solution to two up to four times larger values, depending on how well the deformations can be captured in the signed distance map projections. In the elastoplastic experiment also the dependence of the two parameters A and m via the initial yield strength σ_{y0} played a role. As for any correlation algorithm, physical implications of parameter variations should be taken into account and interdependence of model parameters may lead to poor convergence. Furthermore, improvement of the initial guess robustness is expected if the Gauss–Newton scheme in the algorithm will be replaced by e.g., a modified, constrained minimization approach.

Finally, a step towards real experiments was made. As an ultimate test for the MSC framework, the most rudimentary image segmentation method was explored, i.e. imposing a threshold on the gray level to locate the sample edge, resulting in a pixelized binary image from which the signed distance maps are created. With this image segmentation method, the exact location of the edge is discretely approximated, which reduces convergence. However, convergence was still adequate with a reasonable amount of iterations and with an accuracy of 10^{-4}. Also the influence of misalignment between the camera view in the real experiment and the projection angles used in creating the images from the FE simulation was investigated. It was shown that for angle mismatches up to at least 4° the MSC algorithm still converges towards the solution, however, the accuracy is naturally reduced. Nonetheless, if the projection angles and camera position (in case a perspective projection is made) are incorporated as additional unknown parameters in the correlation, the algorithm robustly converges towards an accurate ($\sim 10^{-4}$) solution, even for very large misalignments up to at least 10° in viewing angle and 50 µm in camera distance. These are promising results for future applications to real experimental images, especially when one of the advanced, (highly) accurate image segmentation methods reported in literature is employed with the MSC method and experimental unknowns, such as projection angles, are added as unknowns in correlation.

Acknowledgments

The research of S.M. Kleinendorst and J.P.M. Hoefnagels was funded by the Netherlands Organization for Scientific Research (NWO) under the VIDI scheme (project number STW12966). The authors greatly acknowledge O. Rokoš and A.M. Oudes for their contribution on image segmentation of real experimental images.

References

[1] G. Hankins, K. Krajnik, B. Galedrige, S. Sakha, P. Hylton, W. Otoupal, Improving safety structures on sprint and midget race cars, SAE Technical paper. 2014-01-0561, 2014, http://dx.doi.org/10.4271/2014-01-0561.

[2] D.R. Drodge, B. Mortimer, C. Holland, C.R. Siviour, Ballistic impact to access the high-rate behaviour of individual silk fibres, J. Mech. Phys. Solids 60 (10) (2012) 1710–1721, http://dx.doi.org/10.1016/j.jmps.2012.06.007.

[3] S.L. Bazhenov, I.A. Dukhovskii, P.I. Kovalev, A.N. Rozhkov, The fracture of svm aramide fibers upon a high-velocity transverse impact, Polymer Sci. 43 (1) (2000) 61–71.

[4] C. Riegel, J.L. Nowinski, An experimental investigation of wave propagation in a rubber string impacted by a projectile, Int. J. Non-Linear Mech. 11 (4) (1976) 229–237, http://dx.doi.org/10.1016/0020-7462(76)90002-0.

[5] M.R. O'Masta, V.S. Deshpande, H.N.G. Wadley, Mechanisms of projectile penetration in Dyneema® encapsulated aluminum structures, Int. J. Impact Eng. 74 (2014) 16–35, http://dx.doi.org/10.1016/j.ijimpeng.2014.02.002.

[6] A. Savov, S.K. Pakazad, S. Joshi, V. Henneken, R. Dekker, A post processing approach for manufacturing high-density stretchable sensor arrays, in: SENSORS, 2014 IEEE Proceedings, 2014, pp. 1703–1705. http://dx.doi.org/10.1109/ICSENS.2014.6985350.

[7] S. Shafqat, J.P.M. Hoefnagels, A. Savov, S. Joshi, R. Dekker, M.G.D. Geers, Ultra-stretchable interconnects for hight-density stretchable electronics, Micromachines 8 (9) (2017) 277, http://dx.doi.org/10.3390/mi8090277.

[8] D.-H. Kim, N. Lu, R. Ma, Y.-S. Kim, R.-H. Kim, S. Wang, J. Wu, S.M. Won, H. Tao, A. Islam, K.J. Yu, T.-I. Kim, R. Chowdhury, M. Ying, L. Xu, M. Li, H.-J. Chung, H. Keum, M. McCormick, P. Liu, Y.-W. Zhang, F.G. Omenetto, Y. Huang, T. Coleman, J.A. Rogers, Epidermal electronics, Science 333 (2011) 838–843, http://dx.doi.org/10.1126/science.1206157.

[9] S.R. Gutbrod, M.S. Sulkin, J.A. Rogers, I.R. Efimov, Patient-Specific flexible and stretchable devices for cardiac diagnostics and therapy, Prog. Biophys. Mol. Biol. 115 (2014) 244–251, http://dx.doi.org/10.1016/j.pbiomolbio.2014.07.011.

[10] L. Klinker, S. Lee, J. Work, J. Wright, Y. Ma, L. Ptaszek, R.C. Webb, C. Liu, N. Sheth, M. Mansour, J.A. Rogers, Y. Huang, H. Chen, R. Ghaffari, Balloon catheters with integrated stretchable electronics for electrical stimulation, ablation and blood flow monitoring, Extreme Mech. Lett. 3 (2015) 45–54, http://dx.doi.org/10.1016/j.eml.2015.02.005.

[11] B. Mimoun, V. Henneken, A. van der Horst, R. Dekker, Flex-to-Rigid (F2R): A generic platform for the fabrication and assembly of flexible sensors for minimally invasive intstruments, IEEE Sens. J. 13 (10) (2013) 3873–3882, http://dx.doi.org/10.1109/JSEN.2013.2252613.

[12] F. Hild, S. Roux, Digital image correlation: from displacement measurement to identification of elastic properties - a review, Strain 42 (2006) 69–80, http://dx.doi.org/10.1111/j.1475-1305.2006.00258.x.

[13] B. Pan, K. Qian, H. Xie, A. Asundi, Two-dimensional digital image correlation for in-plane displacement and strain measurement: a review, Meas. Sci. Technol. 20 (6) (2009) 062001.

[14] P. Cheng, M.A. Sutton, H.W. Schreier, S.R. McNeill, Full-field speckle pattern image correlation with B-Spline deformation function, Exp. Mech. 42 (3) (2002) 344–352, http://dx.doi.org/10.1007/BF02410992.

[15] G. Besnard, F. Hild, S. Roux, Finite-Element displacement fields analysis from digital images: application to Portevin-Le Châtelier bands, Exp. Mech. 46 (6) (2006) 789–803, http://dx.doi.org/10.1007/s11340-006-9824-8.

[16] J. Réthoré, T. Elguedj, P. Simon, M. Coret, On the use of NURBS functions for displacement derivatives measurement by digital image correlation, Exp. Mech. 50 (7) (2010) 1099–1116, http://dx.doi.org/10.1007/S11340-009-9304-Z.

[17] T. Elguedj, J. Réthoré, A. Buteri, Isogeometric analysis for strain field measurements, Comput. Methods Appl. Mech. Engrg. 200 (1–4) (2011) 40–56, http://dx.doi.org/10.1016/j.cma.2010.07.012.

[18] S.M. Kleinendorst, J.P.M. Hoefnagels, C.V. Verhoosel, A.P. Ruybalid, On the use of adaptive refinement in isogeometric digital image correlation, Internat. J. Numer. Methods Engrg. 104 (2015) 944–962, http://dx.doi.org/10.1002/nme.4952.

[19] L. Wittevrongel, P. Lava, S.V. Lomov, D. Debruyne, A self adaptive global digital image correlation algorithm, Exp. Mech. 55 (2) (2015) 361–378, http://dx.doi.org/10.1007/s11340-014-9946-3.

[20] J. Réthoré, A fully integrated noise robust strategy for the identification of constitutive laws from digital images, Internat. J. Numer. Methods Engrg. 84 (6) (2010) 631–660, http://dx.doi.org/10.1002/nme.2908.

[21] J. Neggers, J.P.M. Hoefnagels, M.G.D. Geers, F. Hild, S. Roux, Time-resolved integrated digital image correlation, Internat. J. Numer. Methods Engrg. 103 (3) (2015) 157–182, http://dx.doi.org/10.1002/nme.4882.

[22] P.F. Luo, Y.J. Chao, M.A. Sutton, W.H. Peters, Accurate measurement of three-dimensional deformations in deformable and rigid bodies using computer vision, Exp. Mech. 33 (2) (1993) 123–132, http://dx.doi.org/10.1007/BF02322488.

[23] M.A. Sutton, J.J. Orteu, H.W. Schreier, Image Correlation for Shape, Motion and Deformation Measurement: Basis Concepts, Theory and Applications, Springer, Berlin, Germany, 2009.

[24] K. Han, M. Ciccotti, S. Roux, Measuring nanoscale stress intensity factors with an atomic force microscope, Europhys. Lett. 89 (6) (2010) 66003, http://dx.doi.org/10.1209/0295-5075/89/66003.

[25] S.M. Kleinendorst, J.P.M. Hoefnagels, R.C. Fleerakkers, M.P.F.H.L. van Maris, E. Cattarinuzzi, C.V. Verhoosel, M.G.D. Geers, Adaptive isogeometric digital height correlation: application to stretchable electronics, Strain 52 (4) (2016) 336–354, http://dx.doi.org/10.1111/str.12189.

[26] M.L.M. François, B. Semin, H. Auradou, Identification of the shape of curvilinear beams and fibers, Appl. Mech. Mater. 24–25 (2010) 359–364, http://dx.doi.org/10.4028/www.scientific.net/AMM.24-25.359.

[27] A. Bloch, M. François, J.-C. Thomas, O. Flamand, Monitoring of inflatable structures by using virtual image correlation, in: 7th European Workshop on Structural Health Monitoring, July 8–11, 2014, pp. 686–693.

[28] J. Réthoré, M. François, Curve and boundaries measurement using B-splines and virtual images, Optics Lasers Eng. 52 (2014) 145–155, http://dx.doi.org/10.1016/j.optlaseng.2013.06.018.

[29] I. Carlbom, J. Paciorek, Planar geometric projections and viewing transformations, Comput. Surv. 10 (4) (1978) 465–502, http://dx.doi.org/10.1145/356744.356750.

[30] S.M. Kleinendorst, J.P.M. Hoefnagels, M.G.D. Geers, Mechanical Shape Correlation: a novel integrated digital image correlation approach, in: Advancement of Optical Methods in Experimental Mechanics, in: Conference Proceedings of the Society for Experimental Mechanics Series, vol. 3, 2018, pp. 47–54, http://dx.doi.org/10.1007/978-3-319-63028-1_8.

[31] J. Neggers, B. Blaysat, J.P.M. Hoefnagels, M.G.D. Geers, On image gradients in digital image correlation, Internat. J. Numer. Methods Engrg. 105 (4) (2015) 243–260, http://dx.doi.org/10.1002/nme.4971.

[32] G. Besnard, S. Guérard, S. Roux, F. Hild, A spacetime approach in digital image correlation: Movie-DIC, Optics Lasers Eng. 49 (1) (2011) 71–81, http://dx.doi.org/10.1016/j.optlaseng.2010.08.012.

[33] J. Réthoré, S. Roux, F. Hild, An extended and integrated digital image correlation technique applied to the analysis of fractured samples, Eur. J. Comput. Mech. 18 (3–4) (2009) 285–306, http://dx.doi.org/10.3166/ejcm.18.285-306.

[34] A.P. Ruybalid, J.P.M. Hoefnagels, O. van der Sluis, M.G.D. Geers, Image-based interface characterization with a restricted microscopic field of view, Int. J. Solids Struct. 132–133 (2018) 218–231, http://dx.doi.org/10.1016/j.ijsolstr.2017.08.020.

[35] O. Rokoš, J.P.M. Hoefnagels, R.H.J. Peerlings, M.G.D. Geers, On micromechanical parameter identification with integrated dic and the role of accuracy in kinematic boundary conditions, Int. J. Solids Struct. 146 (2018) 241–259, http://dx.doi.org/10.1016/j.ijsolstr.2018.04.004.

[36] S.M. Kleinendorst, B.J. Verhaegh, J.P.M. Hoefnagels, A.P. Ruybalid, O. van der Sluis, M.G.D. Geers, On the boundary conditions and optimization methods in Integrated Digital Image Correlation, in: Advancement of Optical Methods in Experimental Mechanics, in: Conference Proceedings of the Society for Experimental Mechanics Series, vol. 3, 2018, pp. 55–61, http://dx.doi.org/10.1007/978-3-319-63028-1_9.

[37] T.F. Chan, L.A. Vese, Active contours without edges, IEEE Trans. Image Process. 10 (2) (2001) 266–277, http://dx.doi.org/10.1109/83.902291.

[38] L.A. Vese, T.F. Chan, A multiphase level set framework for image segmentation using the Mumford and Shah model, Int. J. Comput. Vis. 50 (3) (2002) 271–293, http://dx.doi.org/10.1023/A:1020874308076.

[39] I. Blayvas, A. Bruckstein, R. Kimmel, Efficient computation of adaptive threshold surfaces for image binarization, Pattern Recognit. 39 (1) (2006) 89–101, http://dx.doi.org/10.1016/j.patcog.2005.08.011.

[40] S. Joshi, A. Savov, S. Shafqat, R. Dekker, Investigation of fur-like residues post dry etching of polyimide using aluminum hard etch mask, Mater. Sci. Semicond. Process. 75 (2018) 130–135, http://dx.doi.org/10.1016/j.mssp.2017.11.025.

[41] S. Maraghechi, J.P.M. Hoefnagels, R.H.J. Peerling, M.G.D. Geers, Correction of scan line shift artifacts in scanning electron microscopy: An extended digital image correlation framework, Ultramicroscopy 187 (2018) 144–163, http://dx.doi.org/10.1016/j.ultramic.2018.01.002.

[42] S. Maraghechi, J.P.M. Hoefnagels, R.H.J. Peerling, O. Rokoš, M.G.D. Geers, Correction of scanning electron microscope imaging artifacts in a novel digital image correlation framework, Exp. Mech. (2018) (submitted for publication).